Stable C, O and S Isotope Record of Magmatic-Hydrothermal Interactions Between the Falémé Fe Skarn and the Loulo Au Systems in Western Mali

James S. Lambert-Smith[1*], Andrew Allibone[2], Peter J. Treloar[3], David M. Lawrence[2], Adrian J. Boyce[4], Mark Fanning[5]

[1]School of Earth and Ocean Sciences, Cardiff University, Main Building, Park Place, Cardiff, CF10 3AT, UK

[2]Barrick Gold (Holdings) Ltd, 3rd Floor, Unity Chambers, 28 Halkett St., St Hellier, Jersey JE2 4WJ, Channel Islands, UK

[3]School of Natural and Built Environments, Kingston University London, Kingston upon Thames, KT1 2EE

[4]Scottish Universities Environmental Research Centre, East Kilbride, Glasgow, Scotland, G75 0QF

[5]Research School of Earth Sciences, Australian National University, Canberra ACT0200, Australia

***Corresponding author email address: lambert-smithj@cardiff.ac.uk**

Keywords: Stable isotopes; Loulo Mining District; Birimian; Orogenic gold mineralization; Iron skarns

Abstract

The Gara, Yalea and Gounkoto Au deposits of the 17+ Moz Loulo Mining District, largely hosted by the Kofi Series metasediments, are located several kms to the east of the 650 Mt Fe skarn deposits in the adjacent Falémé Batholith. The Au deposits are interpreted to have formed through phase separation of an aqueous-carbonic fluid, which locally mixed with a hypersaline brine of meta-evaporite origin. Recognition of an intrusive relationship between the Falémé Batholith and Kofi Series opens the possibility that the Fe skarns and Au deposits are part of the same mineral system. In this paper, we combine new $\delta^{13}C$, $\delta^{18}O$ and $\delta^{34}S$ data from the Karakaene Ndi skarn, minor Au occurrences along the western margin of the Kofi Series, and zircons within plutonic rocks of the Falémé Batholith with existing data from the Loulo Au deposits, to model the contribution of magmatic volatiles to Au mineralization.

C- and O-isotope compositions of auriferous carbonate-quartz-sulfide veins from the Loulo Au deposits have wide ranges ($\delta^{13}C$: –21.7 to –4.5 ‰ and $\delta^{18}O$: 11.8 to 23.2 ‰), whereas values from carbonate veins in Kofi Series Au prospects close to the Falémé Batholith, and the Karakaene Ndi Fe skarn deposit, have more restricted ranges ($\delta^{13}C$: –16.8 to –3.7 ‰, $\delta^{18}O$: 11.4 to 17.2 ‰ and $\delta^{13}C$ –3.0 ± 1 ‰, $\delta^{18}O$ 12.6 ± 1 ‰, respectively). Kofi Series dolostones have generally higher isotopic values ($\delta^{13}C$: -3.1 to 1.3 ‰ and $\delta^{18}O$: 19.1 to 23.3 ‰). Pyrite from Kofi Series Au prospects adjacent to the Falémé

Batholith, have a wide range of $\delta^{34}S$ values (–4.6 to 14.2 ‰), similar to pyrite from the Karakaene Ndi skarn (2.8 to 11.9 ‰), whereas $\delta^{34}S$ values of pyrite and arsenopyrite from the Loulo deposits are consistently > 6 ‰.

Comparison of the C- and O-isotopic data with water-rock reaction models indicates the Loulo Au deposits formed primarily through unmixing of an aqueous carbonic fluid derived from the devolatilisation of sedimentary rocks with an organic carbon component. Isotopic data are permissive of the hypersaline brine which enhanced this phase separation including components derived from both Kofi Series evaporite horizons interlayered with the dolostones and a magmatic-hydrothermal brine. This magmatic-hydrothermal component is particularly apparent in O-, C-, and S-isotopic data from the Gara deposit and Au prospects immediately adjacent to the Falémé Batholith.

Introduction

Orogenic deposits account for ~30 % of total Au production, reserves, and resources (Frimmel and Hennigh, 2015), making them one of the most important sources of Au globally. Most of these deposits formed from near neutral low salinity aqueous-carbonic fluids at temperatures between 250-400°C in greenschist facies metamorphic terranes (e.g. Groves et al., 1998; Goldfarb et al., 2005; Phillips and Powell, 2010; Goldfarb and Groves, 2015). There is widespread consensus that metasedimentary and / or metabasaltic rocks undergoing metamorphic devolatilization reactions are the ultimate source of the ore fluids in orogenic gold deposits, with the metals scavenged from the same rocks (Henley et al., 1976; Norris and Henley, 1976;Kerrich and Wyman, 1990; Goldfarb et al., 1991; Phillips and Powell, 1993; McCuaig and Kerrich, 1998; Pitcairn et al., 2006, Gaboury, 2013; Tomkins, 2013; Pitcairn et al., 2014; Yardley and Cleverley, 2015; Goldfarb and Groves, 2015; Wyman et al., 2016; Groves et al., 2019). However, speculation remains that some deposits include hydrothermal fluids exsolved from crystallizing magmas (Lawrence et al., 2013a, 2013b; Xue et al., 2013; Treloar et al., 2015; Spence-Jones et al., 2018). Resolving this question is an important part of the development of a holistic mineral system model for orogenic Au deposits (Wyman et al., 2016; Groves et al., 2019).

The 17+ Moz Loulo Au Mining District in the Kédougou-Kéniéba inlier in western Mali and eastern Senegal is one of the most richly endowed orogenic Au districts in the West Africa craton (Fig. 1). It includes three major multi-million ounce deposits, including Gara, Yalea, and Gounkoto and numerous satellite deposits that typically contain <1 Moz Au (e.g., Baboto, Faraba, Loulo 3, Loulo 2, P64, and P129). Small-displacement, discontinuous shear-zones, some of which may have nucleated along earlier fold axial planes. Quartz-tourmaline-altered quartz gritstone units within the Kofi Series siliciclastic, carbonate, and evaporitic rocks host the Au deposits. The western margin of the Kofi Series is intruded and unconformably overlain by high-K plutonic rocks of the Falémé Batholith and related Bambadji Formation volcanic rocks, respectively. Magnetite and hematite-rich endoskarns, which contain > 650 Mt Fe, are present within the Falémé Batholith. Related exoskarns locally extend into the Bambadji Formation and the western-most parts of the Kofi Series, further demonstrating the intrusive relationship between the Falémé Batholith and Kofi Series at the time skarn mineralization occurred.

Despite several detailed studies of the Au deposits (Fouillac et al., 1993; Lawrence et al., 2013a; Lawrence et al., 2013b; Lambert-Smith et al., 2016b; Lambert-Smith et al., 2016c), the ultimate source of fluids and Au in the Loulo mineral system remains uncertain. Lawrence et al. (2013b) proposed a magmatic contribution to auriferous fluids due to the presence of a high-temperature (>400 ºC) hypersaline brine in several deposits. However, Lambert-Smith et al. (2016b) argued against a magmatic source for the brines on the basis of B, S, C, and O isotopic data. In particular, B-isotope data indicate derivation of brines from evaporite units in the Kofi Series (Lambert-Smith et al., 2016c). Nevertheless, the Falémé Batholith and associated skarns intrude and extend into the Kofi Series,

instead of being separated by a terrane boundary (Senegal-Mali Shear Zone), reopens the possibility that the Falémé Fe magmatic-hydrothermal system contributed to Au mineralization at Loulo. Furthermore, Masurel et al. (2017c) report direct overprinting of calc-silicate skarn mineralization by biotite-calcite-quartz ± K-feldspar-tourmaline-actinolite alteration associated with Au mineralisation at the Sadiola Hill Au deposit. The deposit is carbonate-hosted and located in the northern part of the Kédougou-Kéniéba inlier in the vicinity of an intrusive centre correlative with the Falémé Batholith.

The Baqata, Kolya, Kabe West and Gefa (Fig. 2) prospects are hosted in the Kofi Series, less than 2 km from the intrusive contact with the Falémé Batholith. Minor Au-bearing veins are also present within the Falémé Batholith, at the Boboti target. These Au occurrences, within the batholith and midway between the batholith margin and major Au deposits of the Loulo Mining District, provide an opportunity to examine the genetic links between the Falémé Fe skarns (Schwartz and Melcher, 2004) and the Loulo Au deposits. Furthermore, samples from the Karakaene Ndi Fe skarn deposits provide data on the isotopic character of the Fe skarns and any local magmatic-hydrothermal contribution to the Au deposits. Here we use new C, O and S isotope data from these Au occurrences and from the Karakaene Ndi skarn, together with existing isotopic data from Gara, Yalea and Gounkoto (Fouillac et al., 1993; Lawrence et al., 2013b; Lambert-Smith et al., 2016b), as tracers for the source to ore pathways of auriferous fluids. The magmatic contribution, if any, to Au mineralization in the Kofi Series is based on new Sensitive High-Resolution Ion Microprobe (SHRIMP) $\delta^{18}O$ analyses of magmatic zircons recovered from the Falémé Batholith.

Geological Setting

The 2.27 to 2.05 Ga Paleoproterozoic terranes of the southern West African Craton constitute one of the world's leading Au–provinces, with an overall endowment in excess of 350 Moz (Goldfarb et al., 2017; Thebaud et al., in press). Paleoproterozoic rocks are exposed in the Baoulé-Mossi domain, the Kédougou-Kéniéba and Kayes inliers (Fig. 1), and in the eastern Reguibat Rise in North Africa. They include shear-bounded, linear and arcuate belts of volcano-sedimentary rocks ca. 2270-2150 Ma old (e.g. Baratoux et al., 2011), younger sedimentary basins ca. 2135-2095 Ma old (e.g. Taylor et al., 1992; Lebrun et al., 2015), and granitoid-dominated terranes ca. 2190-2060 Ma old (e.g. Hirdes et al., 1992; Parra-Avila et al., 2017) . The volcano-sedimentary belts largely comprise lavas of tholeiitic and calc-alkaline affinity, volcaniclastic rocks, and epiclastic sedimentary rocks. The basins are filled with siliciclastic rocks, including arkoses, greywackes, argillites, arenites, and rare limestones and chemical sediments. Multiple suites of granitoid rocks intrude both the belts and the basins.

The Paleoproterozoic terranes formed, accreted, and were deformed over ~200 Myr (e.g. Perrouty et al., 2012; White et al., 2014; Parra-Avila et al., 2016; Grenholm et al., 2019; Thebaud in press) during the 2266-2140 Ma Eoeburnean , and 2135-2050 Ma Eburnean periods (e.g. Taylor et al., 1992; Dia et al., 1997; Loh et al., 2000; Allibone et al., 2002; Gueye et al., 2007; Hein, 2010; De Kock et al., 2011;

Baratoux et al., 2011; Tshibubudze et al., 2015). Initial volcanism, granitoid emplacement, fold and thrust tectonics, and metamorphism took place during Eoeburnean crustal growth and accretion. The ages of the youngest detrital zircon populations indicate that the sedimentary basins developed from 2135 to 2095 Ma (Davis et al., 1994; Oberthür et al., 1998; Hirdes and Davis, 2002; Vidal et al., 2009; Lebrun et al., 2016). Emplacement of younger granitoid plutons (Parra-Avila et al., 2018; Masurel et al., 2017a), further contractional deformation and metamorphism, late strike-slip deformation, and widespread Au mineralization occurred during the subsequent Eburnean orogeny (Oberthür et al., 1998; McFarlane et al., 2011; Parra-Avila et al., 2015; Fontaine et al., 2017; Fougerouse et al., 2017; Masurel et al., 2017b). Greenschist facies mineral assemblages dominate in most Paleoproterozoic rocks across West Africa, but amphibolite and granulite facies assemblages are present locally within both the Eoeburnean belts and Eburnean sedimentary basins (John et al., 1999; White et al., 2014; MacFarlane et al., 2019). Particularly low geothermal gradients of 10-12° C km^{-1} are consistent with modern subduction processes during Eburnean time in some parts of the craton (Ganne et al., 2011; Block et al. 2015).

Geology of the Loulo Mining District

The Kofi Series comprises metamorphosed immature detrital sedimentary and carbonate rocks deposited after 2120-2100 Ma. The former are dominantly sandstones, wackes, and argillites that include both quartz- and feldspar-rich siliciclastic components. Carbonate lithologies are more abundant in the west, close to the contact with the Falémé Batholith (Fig. 2). These are dominantly dolomitic, with mm to cm-scale marl horizons that contain clasts of fine-grained, sub-angular quartz and feldspar and very fine-grained muscovite. Carbonate lithologies also contain a minor graphitic-argillaceous component, present as mm to sub-mm scale lamellae, or as fine rounded and strained clasts. The Kofi Series sedimentary rocks were tilted upright, tightly folded, cut by reverse faults, and metamorphosed under upper greenschist facies biotite zone conditions during D_1 contractional deformation between ca. 2100-2090 Ma. Later small-scale (< 1 km) folding and development of an associated steeply dipping axial planar cleavage, and Au mineralization occurred during D_2 sinistral transcurrent deformation between ca. 2085 and 2060 Ma (Hirdes and Davis, 2002; Schwartz and Melcher, 2004; Lawrence et al., 2013a; Masurel et al., 2017a; Masurel et al., 2017b). The Falémé Batholith, and associated outlying plutons and dikes, intruded the Kofi Series between 2084 ± 8 Ma and 2075 ± 6 Ma, after inversion of the Kofi Series during D_1 contraction. Outlying dikes of the Falémé batholith at Gounkoto and Gara have been affected by the later stages of hydrothermal activity and syn-Au deformation indicating magmatism occurred during the earlier stage(s) of D_2, prior to mineralisation, but nevertheless part of the same overall D_2 event. While the exact timing of mineralization is yet to be determined, these relationships suggest magmatic activity and Au mineralization were broadly synchronous.

Lawrence et al. (2013a, b) describe two end-member styles of Au mineralization at Loulo, termed Gara- and Yalea-style, respectively. Gara-style deposits are characterized by pyrite dominated ores with metal signatures enriched in Fe-Rare Earth Element (REE)-W and rare base metals. Intense tourmaline alteration, which is atypical of orogenic Au deposits (e.g. Groves et al., 1998), and hypersaline fluid inclusions further characterise this style of mineralization (Lawrence et al., 2013b). Conversely, Yalea-style deposits are As-rich and lack REE and base metal enrichment. Alteration assemblages consist of early quartz-carbonate-albite, overprinted by sericite-chlorite-sulfide-Au (Lawrence et al., 2013a). Fluids are dilute and aqueous-carbonic in character (Lawrence et al., 2013b). The Gounkoto deposit exhibits characteristics in common with both styles, including hypersaline fluid inclusions and As-rich sulfide assemblages (Lambert-Smith et al., 2016b). Satellite deposits and exploration targets in the region display characteristics of either style (Lawrence et al., 2013a; Lambert-Smith, 2014a). All Au and Fe mineralization in the district is associated with moderate to intense albitization, which affects most rock types.

Lawrence et al. (2013b) interpreted fluid inclusion assemblages as representing two distinct end-member fluids: 1) a high T, high-salinity, CO_2-poor, aqueous fluid (~400°C; ~45-55 wt. % NaCl equiv.); and 2) a moderate T, dilute, aqueous-carbonic fluid (270-350°C; <10 wt. % NaCl equiv.). Partial mixing between these fluids at Gara-style ore bodies resulted in retrograde boiling and changes in the physicochemical state of both fluids leading to sulfide mineralization and Au precipitation (Lawrence et al., 2013a, b). At Yalea, the hypersaline fluid is absent and fluid inclusion assemblages feature two immiscible phases derived from phase separation of a dilute aqueous-carbonic fluid (Lawrence et al., 2013b). This likely occurred in response to a combination of fluid-rock interaction, particularly sulfidation, and pressure fluctuations along the brittle-ductile host structures. Stable isotope data from Au-related quartz ($\delta^{18}O$ from 12.9 to 17.4 ‰), dolomite ($\delta^{13}C$ from -21.7 to -4.5 ‰), and pyrite ($\delta^{34}S$ from 5.8 to 15.5 ‰) (Lawrence et al., 2013b) at Gara, Yalea and Gounkoto are generally consistent with fluids being sourced from the devolatilization of Kofi Series metasedimentary rocks (Lambert-Smith et al., 2016b), though $\delta^{18}O$ and $\delta^{13}C$ values partially overlap magmatic fields. Furthermore, B-isotope data from hydrothermal tourmaline indicates a meta-evaporite source for B, implying evaporite devolatilization in the genesis of the hypersaline brine (Lambert-Smith et al., 2016c).

Au and Fe mineralization in the western Kofi series and Falémé Batholith

The minor Au occurrences along the western margin of the Kofi Series at Baqata, Kolya, Kabe West, Boboti and Gefa (Fig. 2) have been described in detail by (Lambert-Smith, 2014a). The key geological characteristics of these occurrences and the larger deposits are summarized in Table 1.

Baqata is located ~6.2 km SE of Gounkoto (Fig. 2). Mineralization is hosted in a package of altered Kofi Series quartz wacke, dolostone, and argillite interbedded with siltstones and sandstones, which dips 60° W and strikes 185°. Bedding is cut by a sub-vertical NNE-striking cleavage which is axial

planar to 100 m-scale SSW plunging asymmetric F_2 folds. The sequence is intruded by 1-10 m thick, variably albitized diorite and monzodiorite dikes, and cut by steeply dipping NNW-striking (80E/350) shear zones. Mineralized rocks include both Gara-style ankerite-quartz-pyrite stockworks in tourmalinized quartz wacke and disseminated pyrite and chlorite-pyrite stringers in albitized dolostone and quartz wacke. Au grades locally reach 13.4 g/t but are discontinuous along strike and down-dip. Like at Gara, accessory Ni-sulfides (e.g. millerite), xenotime, and monazite are present. Gold, tellurobismuthite (Bi_2Te_3), calaverite and bismuth are occluded in pyrite and the gangue.

At Kolya, ~13 km south of Gara, discontinuous zones of mineralized rock that contain up to ~5.8 g/t Au are hosted in a package of argillites, greywackes, tourmalinized quartz wackes, and dolostones, which dips 70° W and strikes 350°. These rocks are folded, cleaved, and cut by shear zones in the same manner as those at Baqata. Dolerite dikes intrude the sedimentary rock package. Mineralized rocks at Kolya comprise chlorite-pyrite veins primarily within the dolerite dikes, and minor hydrothermal breccias and ankerite-quartz-pyrite vein stockworks in tourmalinized quartz wacke. Gold occurs as occluded grains and fracture-fill in pyrite and arsenian pyrite, where it is associated with minor altaite (PbTe), melonite ($NiTe_2$) and tellurobismuthite. Kolya lacks Ni-sulfide phases.

Kabe West is located ~2.5 km south west of Kolya. Gold is hosted in intensely albitized igneous rocks which intrude albitized dolostone, siliciclastic rocks and hydrothermal breccias. Gold grades are typically 2-4 g/t (locally up to 11.3 g/t) and spatially discontinuous. Structural controls on mineralization are not known due to poor exposure, lack of oriented drill core, and overprinting of pre-mineralization fabrics by intense albitization. Pyrite is the dominant ore phase and contains up to 1.9 wt. % Co and 0.5 wt. % Ni. Gold, altaite and melonite occur as inclusions within, or annealed to, pyrite grains, which are disseminated in albitized wall rock and in hydrothermal breccias with tourmaline or dolomite cement.

Mineralized rocks at Gefa, ~7 km south of Baqata, are hosted in a package of albitized argillite, dolostone, and greywacke. The host sedimentary rocks strike N-S and dip 80° W and are intruded by unmineralized diorite and quartz feldspar porphyry dikes. These rocks are cut by sheared polymict hydrothermal breccias. Mineralized rocks are generally characterized by Au grades < 0.5 g/t, localized within zones of brittle quartz-carbonate-pyrite veining that cross cut intensely albitized rock.

Boboti is located ~8.3 km to the south west of Baqata. Mineralization is hosted in albitized subvolcanic andesites and medium to coarse-grained diorites of the Boboti Pluton. Gold is hosted by pyrite grains within carbonate-pyrite veinlets and minor disseminated pyrite in the immediate wall rock to veins. Grades reach a maximum of 2.6 g/t Au, but mineralized zones are rarely continuous over more than 1 meter downhole.

The Falémé Iron District (Schwartz and Melcher 2004) endo- and exoskarn deposits are located within the Falémé Batholith, associated altered Bambadji Formation volcanic rocks, and western-most parts of the Kofi Series (Fig. 2). In the skarns, proximal halos of calc-silicate alteration (actinolite-epidote-allanite-titanite ± clinopyroxene-garnet) overprint regional albitization (Fig.3 a-e). This is further overprinted by massive magnetite ± apatite ore (Fig. 3f). Late sulfide mineralization which typically includes coarse disseminated pyrite and chalcopyrite, or pyrite-chalcopyrite-calcite veins cuts the iron ore (Fig. 3f, g). These sulfides are locally auriferous, typically containing < 0.5 g/t Au and rarely up to 3 g/t Au associated with trace amounts of Co-Ni-U-bearing phases. Preliminary fluid inclusion studies by Schwartz and Melcher (2004) and Lambert-Smith (2014a) tentatively indicate a H_2O-NaCl-CO_2 magmatic fluid, with low salinity (approx. 3.3 wt. % NaCl equiv.) and $XCO_2 = 0.11$. The alteration and ore mineralogy of the skarns share commonalities with Fe-oxide apatite deposits, and their close spatial association with a large orogenic Au camp hints at IOCG affinities (Schwartz and Melcher 2004, Lawrence et al. 2013a).

Sample characteristics and Methods

$\delta^{13}C$ and $\delta^{18}O$ was measured in 28 samples from the Kolya, Baqata, Boboti, Gefa and Kabe West exploration targets and 7 samples from the Karakaene Ndi skarn (Fig. 2). These data include ankerite, calcite and dolomite from auriferous, skarn-related, and barren hydrothermal veins and wall rock alteration, and dolomite from host dolostone units (Fig. 4a). A further 49 $\delta^{13}C$ and $\delta^{18}O$ analyses are included from published data for Gounkoto (Lambert-Smith et al., 2016b); Gara (Fouillac et al., 1993 ; Lawrence et al., 2013b), and Yalea (Lawrence et al., 2013b). $\delta^{34}S$ was measured in 23 pyrite samples from Kolya, Baqata, Boboti and Kabe West exploration targets and in 11 pyrite samples from the Karakaene Ndi skarn. Zircon $\delta^{18}O$ values were measured by SHRIMP on 3 samples of quartz monzodiorite and quartz monzonite from the Falémé Batholith (RG10036, RG10039, RG10050) and one sample of Bambadji Formation andesitic volcaniclastic rock (RG10030).

Mineralized vein characteristics

Tourmalinized quartz wacke units are important ore hosts at Gara and the P-64 satellite, subordinate ore hosts at Gounkoto, and host sub-economic mineralization at the Baqata and Kolya targets. Tourmalinization involves the replacement of the matrices of wackes with cryptocrystalline tourmaline, making the unit more brittle and therefore susceptible to the development of ankerite-quartz-pyrite-Au ± dolomite ± tourmaline hydro fracture vein stockworks (Fig. 4b). These stockworks contain several vein morphologies characteristic of the brittle-ductile environment, including planar centimeter- to millimeter-scale veins and veinlets, brecciated and boudinaged veins, and sigmoidal vein arrays. Veining is typically multi-generational, occurring in multiple orientations and at multiple scales (<100 μm to ~2-3 cm vein width). This stockwork style of mineralization typically affects ~1 to 20 m thick

units and is associated with Au grades up to ~100 g/t. High grades are generally associated with strongly altered host rocks, high carbonate and sulfide content in the veins, and the most intense vein networks with several generations of veins. Veins at Gara commonly include late, gray, quartz-pyrite-Au cores (Lawrence et al., 2013b).

In contrast, veining is a minor part of the mineralized rocks at Yalea and Gounkoto, which include a larger proportion of sulfide stringers, disseminations in the matrix of hydrothermal breccias, and chloritic ductile shear zones. Mineralized veinlets at Yalea cross-cut ductile shear fabrics, and contain arsenopyrite-pyrite-arsenian pyrite-Au ± quartz ± ankerite (Fig. 4c). At Gounkoto quartz-carbonate-pyrite-chlorite veins commonly occur several 10s of meters outside the main ore zone and are associated with grades up to ~5 g/t Au. Veins are typically undeformed and may cross-cut earlier Au mineralization. Mineralogically similar veins have been observed in high grade ore shoots but are typically highly deformed and overprinted by later Au mineralization. Sulfides occupy up to 50 vol. % of the vein assemblage (more typically ~20 %), and carbonate mineralogy is commonly dolomitic and rarely ankeritic. Vein width varies from <100 μm up to 6-7 cm. Many veins have been reactivated and brecciated by later hydrothermal events. Undeformed hydrofracture veins and veinlets are also common at the Baqata, Boboti, Gefa and Kabe West exploration targets.

At the Karakaene Ndi skarn, veining generally postdates the oxide ore. Veins are <1 mm to 6 cm thick and composed of <100 μm to >5 mm calcite-pyrite ± quartz ± chlorite ± Au, with pyrite ≈ calcite (Fig. 3g). Sulfide-rich veins do not show the zoned calc-silicate alteration halos characteristic of primary oxide mineralization.

A small number of veins sampled from the Kofi Series were classified as mineralized based on the presence of sulfide minerals, despite returning fire assay results below detection limit (<0.01 ppm). These veins contain fine pyrite and chalcopyrite in variable abundance. Several of these veins contain only one or two sub-mm-scale grains of pyrite or chalcopyrite (Fig. 4d), while others contain several modal percent of coarse pyrite (some with multiple generations) (Fig. 4g).

Barren vein characteristics

Barren hydrothermal veining occurs throughout the Loulo Mining District (Fig. 4e-f). Pre-mineralization barren quartz-carbonate veins are deformed and display asymmetric fold patterns (Fig. 4f). Late-stage barren quartz-carbonate veins, including at Gara, Yalea, and Gounkoto, cross cut mineralization and alteration (Lawrence et al., 2013a). Elsewhere in the district, similar veining cross cuts barren country rock (Fig. 4e). These late veins are typically undeformed. The timing of veins occurring outside the footprint of the large deposits is somewhat uncertain; it is possible that some of these veins are barren equivalents to mineralized veins. The mineralogy in barren veins comprises

variable proportions of quartz-dolomite ± chlorite, with no sulfide minerals present. Vein width ranges from <1 mm to approximately 8 cm (typically <1 cm).

Analytical procedures

Energy-dispersive X-ray spectroscopy - Mineral compositions were determined using an Oxford Instruments X-ACT Energy Dispersive System detector mounted on a Zeiss EVO 50 Scanning Electron Microscope at Kingston University London. The EDS employed an accelerating voltage of 20 kV, a beam current of 1.5 nA, and a detector process time of 4 seconds. The detection limit for all elements was ~0.2 wt. %.

Stable isotopes in carbonates and pyrite- Carbon and oxygen isotopic analyses of carbonate minerals were carried out at the Scottish Universities Environmental Research Centre (SUERC) in East Kilbride, Scotland. CO_2 was liberated via *in vacuo* reaction with 100 % phosphoric acid at 100 °C for dolomite and ankerite, and at 25 °C for calcite. The CO_2 was analysed on a VG SIRA 10 mass spectrometer. Data were corrected using oxygen fractionation factors for acid-extracted CO_2 at 100 °C of 1.00913 and 1.00901 for dolomite and ankerite, respectively (Rosenbaum and Sheppard, 1986). CO_2 liberated at 25 °C from calcite was corrected using α of 1.0014 (Craig, 1957). Carbon and oxygen isotope data are reported as per mill (‰) deviations relative to Vienna PeeDee belemnite (V-PDB) and Vienna Standard Mean Ocean Water (V-SMOW), respectively. Lab reproducibility based on complete analysis of internal standard MAB 2 (Carrara marble) and replicate analyses of calcite unknowns (including acid digestion at 25 ˚C) was ± 0.10 ‰ for $\delta^{13}C$ and ± 0.12 ‰ for $\delta^{18}O$ (1σ). Reproducibility based on repeat analysis of dolomite unknowns (including acid digestion at 100 ˚C) was ± 0.09 ‰ for $\delta^{13}C$ and ± 0.10 ‰ for $\delta^{18}O$ (1σ).

Pyrite separates were analysed by standard techniques (Robinson and Kusakabe, 1975). SO_2 gas was liberated by combusting sulfides with excess Cu_2O at 1075 °C, in vacuo. Liberated SO_2 was analysed on a VG Isotech SIRA II mass spectrometer, and standard corrections applied to raw $\delta^{66}SO_2$ values to produce $\delta^{34}S$. The data were calibrated using international standards NBS-123 (Sharp, 2017) and IAEA-S-3 (Mann et al., 2009), and the SUERC standard CP-1. Lab reproducibility was ± 0.3 ‰ (1σ). Data are reported in $\delta^{34}S$ notation as per mil (‰) deviations from the Vienna Cañon Diablo Troilite (V-CDT) standard.

Oxygen isotopes in magmatic zircons- Zircon $\delta^{18}O$ values were measured by SHRIMP on 3 samples of quartz monzodiorite and quartz monzonite from the Falémé Batholith (RG10036, RG10039, RG10050) and one sample of Bambadji Formation andesitic volcaniclastic rock (RG10030) (Fig. 2). Descriptions of these rocks and the associated U-Pb zircon geochronology are provided by Allibone et al. (in press). Oxygen ($^{18}O/^{16}O$) isotope ratios were measured for a selection of magmatic areas within zircon grains in order to characterize the isotopic composition of the magma from which they crystallized and thereby

investigate the nature of the source(s) of these magmas. Following the U-Pb analyses, the SHRIMP U-Pb pits, 1-2 µm deep, were lightly polished away and oxygen isotope analyses were made in exactly the same location using SHRIMP II fitted with a Cs ion source and an electron gun for charge compensation as described by Ickert et al. (2008). Oxygen isotope ratios were determined in multiple-collector mode using an axial continuous electron multiplier (CEM) triplet collector, and two floating heads with interchangeable CEM - Faraday Cups. The FC1 (Duluth Gabbro) reference zircons were analyzed to monitor and correct for isotope fractionation. The measured $^{18}O/^{16}O$ ratios and calculated $\delta^{18}O$ values have been normalized relative to a FC1 weighted mean $\delta^{18}O$ value of 5.61 ‰ (Fu et al., 2015). Reproducibility in the FC1 reference zircon $\delta^{18}O$ value was ± 0.40 ‰ (2σ uncertainty) for the analytical session. Temora 2 reference zircons were analysed in the same session as a secondary reference and gave a $\delta^{18}O$ value of 8.04 ± 0.37 ‰, in agreement with that reported by Ickert et al. (2008).

Results

Sulfur isotopes

Sulfur isotope data are listed in full in Table 2. Auriferous sulfides from the Loulo Au deposits and their satellites have $\delta^{34}S$ values between 5.8 and 15.5 ‰, with a mean of 9.6 ‰ (n=74) (Fig. 5a) (Fouillac et al., 1993; Lambert-Smith et al., 2016b; Lawrence et al., 2013b). Diagenetic pyrite from the Kofi series shows a broad range from 6.4 to 25.1 ‰. New $\delta^{34}S$ data (Fig. 5b) from Kabe West ranges from -4.6 to 3.4 ‰ (n=9; mean of -0.4 ‰). Sulfides at Baqata range from 5.5 to 11.8 ‰ (n=4; mean of 8.1 ‰). Kolya exhibits $\delta^{34}S$ values from 4.2 to 14.2 ‰ (n=5; mean of 9 ‰). Mineralization at Boboti ranges from 1.7 to 3.9 ‰ (n=5; mean of 2.5 ‰). Sulfides at the Karakaene Ndi skarn range from 2.8 to 11.9 ‰ (n=11; mean of 5.3 ‰) (Fig, 5c). Early sulfides disseminated within the massive Fe ore and hosted in Fe oxide veins range from 2.8 to 4.4 ‰, whereas late sulfide-rich veins range from 4.9 to 11.9 ‰.

Carbon isotopes

Carbon isotope data are listed in full in Table 3. The $\delta^{13}C$ values for carbonate country rocks, and barren and mineralized veins in the Loulo Mining District range from -21.7 to 3.8 ‰ (mean of -7.3 ‰; n=79). The dataset for Au-bearing veins exhibits peaks in $\delta^{13}C$ at -10 ‰, -6 ‰ and at 0 ‰ (Fig. 6a). Data from Kofi Series dolostones provide a local $\delta^{13}C$ values for carbonate country rocks. These range from -3.1 to 1.3 ‰ (mean of -0.5 ‰; n=10).

Sulfidized carbonate-bearing veins in the Kofi Series show a broad range in $\delta^{13}C$ values from -21.7 to -3.7 ‰ (n=55) (Fig. 6a). This population is largely unimodal, with a minor negative skew toward lower $\delta^{13}C$ values (mode at approximately -8 ‰). The Bambadji exploration targets (Fig. 6b) show a range in $\delta^{13}C$ from -16.8 to -3.7 ‰ (mean of -8.4 ‰; n=13). Baqata veins range from -15.0 to -3.7 ‰ (mean of -8.6 ‰; n=6). Kolya veins range from -8.8 to -5.1 ‰ (mean of -7.7 ‰; n=5). Kabe West ranges from -

8.6 to -5.9 ‰ (mean of -7.4 ‰; n=6). Gefa ranges from -16.8 to -7.0 ‰ (mean of -10.2 ‰; n=4). Gara, Yalea, and Gounkoto show the greatest range of values, from -21.7 to -4.5 ‰ (mean of -11.6 ‰; n=32). Gara shows a range from -14.4 to -4.5 ‰ (mean of -9.6 ‰; n=16), Yalea from -21.7 to -10.6 ‰ (mean of -16.7 ‰; n=8), and Gounkoto from -13.6 to -6.3 ‰ (mean of -9.1 ‰; n=8). In contrast, barren (sulfide absent) carbonate-bearing hydrothermal veins show a similar population distribution to carbonate country rocks. This ranges from -2.4 to 3.8 ‰ (mean of -0.7 ‰; n=9) (Fig. 6a). Calcite from sulfide veins at the Karakaene Ndi skarn deposit range from -4.1 to -1.8 ‰ (n=7; mean of -3.0 ‰) (Fig. 6c).

Oxygen isotopes in carbonates

Oxygen isotope data for carbonate minerals are listed in full in Table 3. The O isotope ratios of carbonates in the Loulo district exhibit a wide range from 11.4 to 23.3 ‰ (n=79). The data are not normally distributed and have a positive skew toward higher $\delta^{18}O$ values (Fig. 6d). Kofi series limestones tend to exhibit heavier $\delta^{18}O$ values than hydrothermal veining, ranging between 19.1 and 23.3 ‰, with one outlying value at 15.1 ‰ (mean of 20.3 ‰; n=10). Barren hydrothermal veins are indistinguishable from mineralized hydrothermal veins based on their O-isotopic composition (Fig. 6e). Barren veins range from 11.7 to 21.1 ‰ (mean of 15.8 ‰; n=14). Mineralized veins range from 11.4 to 23.2 ‰ (mean of 15.6 ‰; n=55). Calcite from sulfide veins at the Karakaene Ndi skarn deposit range from -12.0 to -13.5 ‰ (n=7; mean of -12.6 ‰) (Fig. 6f).

Oxygen isotopes in magmatic zircons

Oxygen isotope data in magmatic zircons is listed in full tin Appendix Table A1. The zircon $\delta^{18}O$ values obtained from Bambadji Formation andesitic volcaniclastic rock sample RG10030 range between 6.4 and 8.4 ± 0.5 ‰ with a weighted mean value of 7.2 ± 0.7 ‰ (MSWD of 13). However, a probability density plot shows a minor mode at around 6.5 ‰, with scatter among higher values. All grains analysed have U-Pb isotopic ratios < 10% discordant implying their oxygen isotope ratios are unlikely to have been markedly affected by post crystallisation Pb-loss ref.

Zircons from two samples of the Highway Pluton (RG10036, RG10039) were analysed.. The 5 most concordant zircon analyses in RG10036 have $\delta^{18}O$ ratios of between 7.0 and 8.4 ± 0.5 ‰. The two most concordant analyses from RG10039 have associated $\delta^{18}O$ ratios of 7.0 and 8.1 ± 0.5 ‰, respectively. Remaining discordant zircons from these two samples have $\delta^{18}O$ ratios (6.5 to 8.4 ‰), which are in broad agreement with the range of values in concordant zircons in all the samples (6.4 to 8.4 ‰) and may therefore be considered with the other data. The weighted mean for RG10036 is 7.9 ± 0.4 ‰ (MSWD of 8.4). RG10039 has too few analyses to be significant, though the weighted mean of 7.7 ‰ is in broad agreement with data from the other samples. A sample from the Balangouma Pluton, west of Gara (RG10050), contains relatively abundant concordant zircon whose $\delta^{18}O$ ratios range between 6.5 and 8.1 ± 0.5 ‰ with a mean of 7.6 ± 0.3 ‰ (MSWD of 3.8).

A weighted mean of all the zircon data yields a $\delta^{18}O$ value of 7.6 ± 0.2 with an MSWD of 8.2. However, aA probability density plot of the entire dataset suggests that there are two general values recorded, with a major mode at : a more prominent value around 7.9 ± 0.1 ‰ and a less prominent lower valueminor mode around 6.7 ± 0.2‰.

Discussion

S-isotope Compositions and Sulfur Sources

New $\delta^{34}S$ data from the Au occurrences at Kabe West, Baqata, Boboti, and Kolya (-4.6 to 14.2 ‰) partially overlap the range of values for the Loulo Au deposits (5.8 to 15.5 ‰) and those of diagenetic pyrite from the Kofi series (6.4 to 25.1 ‰), though they also extend to lower ratios (Fig. 5 a and b). Lambert-Smith et al. (2016b) interpret these data to indicate that sulfur in the main Loulo Au deposits is derived from a metasedimentary source. Sulfides at the Karakaene Ndi Fe skarn change from lower isotopic values in early disseminated sulfides (2.8 to 4.4 ‰), to higher values in late sulfide-rich veins (4.9 to 11.9 ‰), which overlap with the range of $\delta^{34}S$ in Kofi series diagenetic pyrite (Fig. 5c). This suggests that paragenetically early sulfur in the skarn was dominantly sourced from magmatic fluids ($\delta^{34}S$ = 0±2 ‰) (Ohmoto, 1972), but as the hydrothermal system developed, sulfur with high $\delta^{34}S$ (> 4 ‰) was incorporated from the Kofi series metasedimentary rocks or the Bambadji Formation volcanic rocks. Persistently low $\delta^{34}S$ values at the Boboti and Kabe West Au prospects (-4.6 to 3.9 ‰) imply a magmatic sulfur source.

C-isotope Compositions and Carbon Sources

Carbonate minerals from barren hydrothermal veins and dolostone country rocks throughout the southern Kofi Series have $\delta^{13}C$ values between -3.1 ‰ and 3.8 ‰ (Fig. 6a, b), with means of -0.7 and -0.5 ‰, respectively. These values are typical for Paleoproterozoic marine carbonate (Strauss and Moore, 1992). This indicates that barren veins likely formed through dissolution of carbonate minerals in the host sedimentary rocks (Dietrich et al., 1983; Elmer et al., 2006; Lawrence et al., 2013b). Compositions of auriferous veins in the Kofi Series are more heterogeneous, ranging from -21.7 to -3.7 ‰ (mean of -9.9 ‰) (Fig. 6a, b). The lowest ratios at Yalea (-19.5 to -21.7 ‰) (Lawrence et al., 2013b), are within the $\delta^{13}C$ range of Precambrian organic matter, at -24.7 ± 6 ‰ (Schidlowski et al., 1975, Papineau et al., 2010). This is similar to carbonaceous material in of the Paleoproterozoic Kumasi Basin in Ghana, which yield mean $\delta^{13}C_{org}$ of -23 ± 5 ‰ (Mumin et al., 1996; Oberthuer et al., 1996). The $\delta^{13}C$ of auriferous veins from elsewhere in the Loulo district, including most data from Baqata, Kolya, Kabe West and Gefa (Fig. 6b), fall between -16 and -4 ‰. These higher values could reflect contributions of carbon from either (1) the Kofi Series dolostones or (2) magmatic CO_2 ($\delta^{13}C_{CO2} \approx$ -5 to -10 ‰; Ohmoto, 1972).

In either case, the range of compositions indicate a contribution of ^{13}C-depleted organic carbon to the hydrothermal system (Fig. 6a). The two most probable mechanisms by which this might occur are: 1) oxidation of graphite derived from organic matter ($C + O_2 \rightarrow CO_2$), or 2) hydrolysis of graphite ($2C + 2H_2O \rightarrow CO_2 + CH_4$). Application of isotopic fractionation factors (using the equations of Ohmoto and Rye, 1979; Golyshev, et al. 1981; Horita, 2001) for average ore forming temperatures in the Loulo district (ca. 320 °C; Lawrence et al., 2013b; Lambert-Smith et al., 2016b) suggests that *in situ* hydrolysis of graphite in Kofi dolostones would produce CO_2 with $\delta^{13}C \geq -17.5$ ‰. Carbonate minerals precipitated from this fluid between 295 and 340 °C (after Lawrence et al 2013b) would have $\delta^{13}C$ between of –18.1 and -19.2 ‰. This cannot therefore explain the lowest $\delta^{13}C$ values at Yalea. Alternatively, C-isotope fractionation during hydrolysis could occur in the fluid source region. A fluid with $X(CO_2) = 0.2$-0.3 may be produced at temperatures of 500 to 520 °C at the greenschist-amphibolite transition (Elmer et al., 2006). This could produce $\delta^{13}C_{CO2}$ values as low as -20.8 ‰ yielding $\delta^{13}C_{dolomite}$ as low as -21.7 ‰, depending on the initial $\delta^{13}C_{org}$ of the source material. In both cases we assume open system behaviour, whereby CO_2 has undergone significant fractionation from the source graphite composition. This ^{13}C-depleted fluid may then have interacted with country rocks in the Kofi Series or a fluid (brine?) of differing composition, to produce the wide range of observed values.

The isotopic compositions of late carbonate-sulfide veining at the Karakaene Ndi Fe skarn deposit (-4.1 to -1.8 ‰) are ~1 ‰ above the expected range of values for a magmatic fluid (Fig. 6c). A cooling magmatic fluid should precipitate carbonate minerals with lower $\delta^{13}C$; therefore, it seems likely that fluid mixing or wall rock interaction have modified the fluid. The most likely scenario is incorporation of heavier $\delta^{13}C$ from the Kofi dolostones during hydrothermal activity around the skarn (Fig. 6a, c). This is consistent with the interpretation of the $\delta^{34}S$ data (Fig. 5a, c).

O-isotope Compositions and Oxygen Sources

The $\delta^{18}O$ values in hydrothermal carbonate veins in the Kofi Series are more homogeneous compared with the $\delta^{13}C$ values. Barren, sulfidized and auriferous veins have near identical mean $\delta^{18}O$ values of 15.8, 15.0, and 15.6 ‰, respectively, and range from 11.4 to 23.2 ‰ (Fig. 6 d, e, f). Isotopic compositions above ~18 ‰ in auriferous veins are interpreted to represent disequilibrium as $\delta^{18}O$ in paired quartz-dolomite samples at Gounkoto and Yalea display $\delta^{18}O_{quartz} < \delta^{18}O_{dolomite}$ (Lambert-Smith et al., 2016b; Lawrence et al., 2013b). This scenario suggests later modification of $\delta^{18}O_{dolomite}$ (Jenkin et al., 1991). Most samples with $\delta^{18}O$ below ~14 ‰ are from the western Kofi Au prospects (Fig. 6d and e), which show relatively high $\delta^{13}C$ values >-10 ‰ (Fig. 6b).

O-isotope compositions for Falémé batholith magmatic rocks are constrained by $\delta^{18}O_{zircon}$ data obtained via SHRIMP analysis, the dominant population of which yield a $\delta^{18}O_{zircon}$ value of 7.9 ± 0.1 ‰ (2 SD; n=28) (see App. Table A1). We estimated $\delta^{18}O_{magma}$ using melt-zircon fractionation values of Trail et

al. (2009) ($\Delta_{melt\text{-}zircon}$ at 800 °C = 1.7 ‰). We then applied the plagioclase-water fractionation values of Zheng (1993) ($\Delta_{albite\text{-}H2O}$ at 700 °C = 0.2 ‰), to calculate a $\delta^{18}O_{H2O}$ value of 9.4 ‰ for the Falémé batholith. Zircon crystallisation temperatures were estimated using data in Samperton et al. (2017). The maximum range of $\delta^{18}O_{H2O}$ values for a magmatic-hydrothermal fluid exsolved from the Falémé batholith is 7.9 to 10.0 ‰. The average $\delta^{18}O_{fluid}$ value calculated from carbonates in the Loulo district overlaps this range at 10.2 ± 2.3 ‰ (calculated at 320 °C using the equations of Zheng, 1999). However, these data alone cannot constrain the fluid source as $\delta^{18}O_{fluid}$ values for local magmatic and metamorphic water (~4 to 25 ‰) overlap (Sheppard, 1986). At best these data are permissive of either, or both, fluid sources, and so must be interpreted in their geological context, together with $\delta^{13}C$ data. The western Kofi Au prospects have lower average $\delta^{18}O_{fluid}$ values of 9.1 ‰ (Baqata), 8.6 ‰ (Kolya), 8.3 ‰ (Kabe West), and 8.5 ‰ (Gefa), whereas the intrusive-hosted Boboti target has a significantly lower value of 6.6 ‰. These lower values suggest the involvement of fluids sourced from the Falémé batholith in Au mineralization at these locations. Similarly, $\delta^{18}O_{calcite}$ at Karakaene Ndi, at temperatures of 550 °C, yield a $\delta^{18}O_{fluid}$ range from 9.6 to 11.1 ‰, overlapping the upper end of local magmatic water values.

Carbon-Oxygen Isotope Modelling

To test whether magmatic fluids may have contributed to the Au-bearing hydrothermal system of the Loulo district , we calculated the C-O isotope compositions of mixtures between a dilute metamorphic aqueous-carbonic fluid, and 1) a hypersaline brine derived from metaevaporites, and 2) a magmatic hydrothermal fluid sourced from the Falémé batholith. The equations of Schwinn et al. (2006) were used to calculate $\delta^{13}C$ values for carbonates precipitated from a mixed fluid ($\delta^{13}C_M$):

$$\delta^{13}\mathrm{C_M} = \left(\frac{m_\mathrm{B}^* f_\mathrm{B}}{m_\mathrm{B}^* f_\mathrm{B} + m_\mathrm{AC}^*(1 - f_\mathrm{B})}\right) \cdot \delta^{13}\mathrm{C_B} + \left(\frac{m_\mathrm{AC}^*(1 - f_\mathrm{B})}{m_\mathrm{B}^* f_\mathrm{B} + m_\mathrm{AC}^*(1 - f_\mathrm{B})}\right) \cdot \delta^{13}\mathrm{C_{AC}}$$

Where $\delta^{13}C_B$, $\delta^{13}C_{AC}$, and represent C-isotope compositions for the brine, the aqueous-carbonic fluid, respectively. The molalities of carbon in the brine m_B* and aqueous-carbonic fluid m_{AC}*, have been calculated using the following equation:

$$m_\mathrm{B}^* = \frac{m_\mathrm{B}}{\left(n_\mathrm{W} + \sum m_{i,\mathrm{B}}\right)}$$

where n_w is the total number of moles H_2O in 1 kg water, m_B is the uncorrected molality of carbon in the brine, and $\sum m_{i,B}$ is the sum of the molalities of all solutes in the brine. This approach considers the significant salinity differences between the two fluids by correcting for total solute concentrations (Schwinn et al., 2006). These equations were adapted to model $\delta^{18}O_{fluid}$.

End member fluid isotopic and chemical compositions are detailed in Table 4. The starting isotopic composition for the brine ($\delta^{13}C_{fluid}$ = 1.8 ‰ and $\delta^{18}O_{fluid}$ = 17.3 ‰) is based on devolatilization of a

dolostone with similar initial $\delta^{13}C$ and $\delta^{18}O$ to that of Kofi Series dolostones (Valley, 1986). Starting compositions of the magmatic fluid ($\delta^{13}C_{fluid}$ = -6.0 ‰ and $\delta^{18}O_{fluid}$ = 9.4 ‰) are based upon $\delta^{18}O_{H2O}$ from the Falémé batholith (App. Table A1) and the accepted range of magmatic $\delta^{13}C_{CO2}$ (Taylor, 1974). The aqueous-carbonic fluid is assumed to have the composition $\delta^{13}C_{fluid}$ = -27.0 ‰ and $\delta^{18}O_{fluid}$ = 10.2 ‰. This represents a fluid derived from metamorphic devolatilization of C_{org} bearing sediments. $\delta^{13}C$ and $\delta^{18}O$ of dolomite were calculated at ore forming temperatures of 320 °C.

Figure 7 shows that the isotopic character of auriferous hydrothermal veins at Loulo cannot be explained by binary mixing between end members of metamorphic aqueous-carbonic fluid and either a meta-evaporite derived brine, or a magmatic fluid from the Falémé batholith. We note above that the isotopic signature of the unequivocally magmatic Karakaene Ndi skarn does not correspond directly to Falémé magmatic fluid values. This suggests that any magmatic-hydrothermal fluid in even the most proximal parts of the hydrothermal system may be somewhat cryptic. We have therefore modelled the effects of water-rock reaction on the C-O isotope system (Fig. 7), with the objectives of (1) explaining the $\delta^{13}C$ and $\delta^{18}O$ signature of the Karakaene Ndi skarn and (2) investigating the magmatic contributions to the Loulo Au deposits, particularly the prospects in the western Kofi Series. This was accomplished using the following equation, assuming open system behaviour (modified after Shelton, 1983):

$$\delta_r^f = \left(\delta_r^i - \delta_w^i + \Delta\right)e^{\frac{-Wc_w}{Rc_r}} + \delta_w^i - \Delta$$

Where $_r$ and $_w$ denote rock and water (or mineral and fluid), respectively. $\delta^i$and δ^f denote the initial and final isotopic composition, respectively. Δ is the fluid-mineral per mil fractionation as a function of temperature (in this case 320 °C for the metamorphic fluid and 550 ˚C for the magmatic-hydrothermal fluid). *C* indicates concentration, *R* mass of rock, and *W* mass of water. The reaction curves were modelled for water-rock ratios between 100 and 0.01. The metamorphic fluid was modelled at XCO_2 = 0.2, and the magmatic-hydrothermal fluid at 0.11 (Lambert-Smith et al., 2016b, Lawrence et al., 2013b). End member fluid isotopic and chemical compositions are as detailed above (Table 4). Average Kofi dolostone compositions were used for the host rock.

Interactions between the Loulo and Falémé Mineral Systems

Carbonate veins from Karakaene Ndi fall along water-rock reaction pathways typical of magmatic-hydrothermal systems (Fig. 7) (e.g. Pass et al., 2014). These data represent a hot (~550 °C) magmatic fluid from the Falémé Batholith interacting with significantly cooler carbonate-rich wall rocks with high $\delta^{13}C$. This pattern is replicated in $\delta^{34}S$ data (Fig. 5c), where a shift to higher $\delta^{34}S$ in later veins suggests an influx of wall rock sulfur as the hydrothermal system began to cool and retrograde skarn mineralization began.

C-O isotope modelling indicates that water-rock reaction between a metamorphic fluid and carbonate-rich Kofi Series host rocks was an important process at Gara, Yalea and Gounkoto and can partly explain the C and O isotopic compositions of these deposits (Fig. 7). Critically, the three world class deposits at Loulo show limited isotopic evidence for direct contribution of magmatic volatiles, with the possible exception of Gara (Fig. 7). In contrast, the Au prospects in the western Kofi Series at Baqata, Kolya, Kabe West and Gefa (as well as limited data points from Gara) have higher $\delta^{13}C$ and lower $\delta^{18}O$ values than the main Loulo deposits, which fall between the aqueous carbonic fluid-dolostone and magmatic brine-dolostone reaction curves (Fig. 7).

On the basis of these data, we suggest that mineralization in the small Au prospects adjacent to the margin of the Falémé Batholith was deposited from a mixed aqueous-carbonic and magmatic fluid, both of which had been modified through reaction with Kofi Series dolostone and/or Bambadji Formation volcanic rocks prior to mixing. While isotopic values for the Kolya, Baqata and Gefa prospects are largely in agreement with those of the main Loulo Au deposits, including their low $\delta^{34}S$ values (Fig. 5a, b), those for Kabe West and Boboti plot at lower $\delta^{18}O$, implying a stronger magmatic-hydrothermal affinity (Fig. 6b and 7). Kabe West and Boboti are both hosted within intensely albitized igneous rocks on the margin of the Falémé batholith, which is intruded by multiple generations of small-scale dikes and stocks consistent with an elevated contribution of magmatic volatiles. Furthermore, low $\delta^{18}O$ values at Baqata, Kolya, and Gefa are consistent with the presence of thin diorite dikes within 5 m of mineralization (Lambert-Smith, 2014a). These dikes may have exsolved small aliquots of magmatic-hydrothermal fluid similar to those responsible for skarn alteration, resulting in the heterogeneous isotopic signature of Au prospects in the western Kofi Series. It should also be noted that some of the isotopic values for hydrothermal minerals in the western Kofi Au prospects could be generated simply from a cooling end-member magmatic fluid.

Metallogenic Model for the Loulo District

Lambert-Smith et al. (2016c) reported that pre-ore hydrothermal tourmalines at Gara and Yalea North were deposited from an ^{11}B-rich fluid whose isotopic character was comparable with metaevaporite source rocks. While evaporite beds have not been identified in the Kofi series, the B-isotope data suggest the marly dolostones in the west of the Kofi basin may have contained evaporitic horizons (Fig. 8a). The Falémé batholith intruded these marly dolostones and evaporite horizons (Fig. 2) between 2084 ± 8 Ma and 2070 ± 5 Ma, during which time the Falémé skarns also formed (Fig. 8 b and c). Field relationships between albitization and magmatic rocks in the Kofi Series suggest NaCl, CO_2 and B were initially mobilized during syn-D_1 metamorphism of Kofi Series dolostones, before Falémé magmatism, giving rise to a paragenetically early brine and widespread associated albitic and tourmaline alteration. Falémé magmatism now seems likely to have contributed both heat and magmatic-hydrothermal fluid to this evolving system, synchronous with on-going D_2 metamorphism and minor transcurrent

deformation. These magmatic fluids may have evolved into high temperature saline brines through reaction with the dolostones or mixing with a metamorphic brine derived from earlier devolatilization of the dolostones and interbedded evaporites. This scenario would explain both the high fluid temperatures (>400 °C) documented by Lawrence et al. (2013b) and the meta-evaporite B-isotope signature described by Lambert-Smith et al. (2016c), as it seems likely that the dominant B reservoir in such a scenario would be the evaporative wall rocks.. High thermal gradients and permissive structural architecture allowed widespread circulation of this hybrid magmatic-hydrothermal and meta-evaporitic brine, resulting in on-going, multi-phase, district-scale Na and B metasomatism prior to and during Au mineralization (Lawrence et al., 2013b; Lambert-Smith et al., 2016a; Lambert-Smith et al., 2016b; Lambert-Smith et al., 2016c) (Fig. 8b). At the Karakaene Ndi skarn high $\delta^{34}S$ and $\delta^{13}C$ values suggest a contribution to the hydrothermal system from wall rocks with isotopic characteristics similar to the Kofi dolostones. Similarly, at Gara a shift from high $\delta^{11}B$ (~12.7 ‰) to lower values (~5 ‰) indicates that in places, brines containing both evaporite and magmatic components (hybrid) mixed with more dilute aqueous-carbonic fluids during Au mineralization (Lambert-Smith et al., 2016c). This implies that the hybrid brine contributed to the formation of both the Falémé skarns and the Loulo Au deposits.

Given that the aqueous-carbonic fluid is present in all Au deposits in the Loulo region, whereas the hypersaline brine is absent at Yalea, it seems likely that the former was more important in terms of introducing Au to the system. Stable isotope data from Au-related pyrite and arsenopyrite ($\delta^{34}S$ 5.8 to 9.6 ‰), quartz ($\delta^{18}O$ 15.8 to 16.3 ‰ yielding a mean $\delta^{18}O_{fluid}$ of approx. 9.7 ‰ at 320 °C) , dolomite ($\delta^{13}C$ -15.8 to -21.7 ‰) (Lawrence et al., 2013b) and tourmaline ($\delta^{11}B$ -0.5 to 9.3 ‰) (Lambert-Smith et al., 2016c) at Yalea are all compatible with the aqueous-carbonic fluid being sourced from Kofi Series siliciclastic metasedimentary and carbonate rocks (Rye and Ohmoto, 1974; Sheppard, 1986; van Hinsberg et al., 2011) with a significant organic C component (Schidlowski et al., 1975). Our new data and modelling show that the brine with which the aqueous-carbonic fluid mixed is likely to have evolved from interaction between magmatic-hydrothermal fluid(s) and the Kofi Series dolostones (± meta-evaporites). Heat from the intrusion of the Falémé Batholith could conceivably have perturbed the local geothermal gradient sufficiently to drive this district scale hydrothermal system.

Implications for Orogenic Au and other Hydrothermal Systems

Our data suggest that magmatic fluids can make a significant contribution to some orogenic Au mineralization. In the Loulo example magmatism, combined with highly reactive dolostone and evaporitic country rocks resulted in generation of a hybrid brine that appears to have acted as a chemical trap for this and other aqueous carbonic Au-bearing fluids.

Comparisons between the Loulo District and some iron oxide Cu-Au (IOCG) provinces are also instructive. Deposits of the Carajás Mineral Province of northern Brazil are somewhat analogous in that they feature hypersaline brines (up to 58 wt. % equiv. NaCl) (da Costa Silva et al., 2015), which have

derived their salt content from meta-evaporitic rocks (Xavier et al., 2008; Riehl and Cabral, 2018). Intrusion of magma into evaporite bearing rocks has set up district-scale hydrothermal systems resulting in abundant sodic and calcic alteration. Schwartz and Melcher (2004) and Lawrence et al. (2013a) have both suggested that the Falémé skarns share characteristics with IOCG deposits. Notably, the skarns are rich in low-Ti iron oxides and are associated with widespread and paragenetically early alteration associated with both CO_2-rich and saline fluids. The Falémé skarns however, differ in that they contain no economic Cu, only relatively low-grade Au, and are more intimately associated with magmatic rocks than is typical for IOCG deposits (c.f. Williams et al., 2005).

The isotopic data largely supports a metamorphic devolatilization model for the system at Loulo (e.g. Groves et al., 2019). Though the term may not be wholly appropriate in describing the Loulo deposits, there is a clear metamorphic signature in the isotope data with deposits such as Yalea formed largely without the influence of the hybrid magmatic-hydrothermal/evaporite-derived brine.

Conclusions

Taken together, our data suggest a critical role for magmatism in the development of early alteration assemblages in the Loulo District, in the genesis of the Falémé iron skarns, and in those Au deposits that formed in response to fluid mixing. In these deposits, including Gara and the minor Au occurrences in close spatial association with dikes and sills on the margin of the Falémé Batholith, there is strong indications that evolved magmatic fluids were present during mineralization.

We envisage a scenario where the Falémé Batholith intrudes the marly evaporite-bearing carbonate rocks of the western Kofi Series. Fluids exsolved from the Falémé Batholith interacted with the marly dolostones generating a hypersaline brine which circulated through the Kofi and Falémé lithologies. This resulted in the widespread albitization and tourmalinization characteristic of the region, which hardens certain lithologies providing a favourable competency contrast for Au-bearing fluids to exploit. Early metasomatism is overprinted by orogenic-style Au and Fe skarn mineralization; the former related to the incursion of aqueous-carbonic fluids. These fluids largely precipitate minerals due to pressure fluctuations or water-rock reactions (Lambert-Smith et al., 2016b, Lawrence et al., 2013b), but in places partially mix with the magmatic-evaporitic brines which provide a chemical trap for Au mineralization. In this way, the intrusion of the Falémé Batholith played a direct role in the development of the Loulo Au mineral system. Skarn formation is likely to have been promoted by the presence of Cl-rich brines, which would have encouraged metal transport in $FeCl_2$ complexes.

Acknowledgements

This research was funded by Randgold Resources and Kingston University. Isotopic analyses were carried out through a NERC Facilities Grant (IP-1252-0511). A. J. Boyce is funded by NERC support

to the Isotope Community Support Facility at SUERC. The authors wish to thank the technical staff at SUERC and Kingston for their assistance in carrying out sample preparation and analysis. SHRIMP zircon oxygen isotope data was acquired by Mark Fanning using the facilities at the Australian National University as part of a collaborative program funded by Randgold Resources Ltd during 2014-2015. We also wish to thank Larry Meinert and two anonymous reviewers for their constructive reviews, which undoubtedly improved the manuscript.

References

Allibone, A., Teasdale, J., Cameron, G., Etheridge, M., Uttley, P., Soboh, A., Appiah-Kubi, J., Adanu, A., Arthur, R. and Mamphey, J., 2002, Timing and structural controls on gold mineralization at the Bogoso gold mine, Ghana, West Africa: *Economic Geology,* v. 97**,** p. 949-969.

Allibone, A., Lawrence, D., Scott, J., Fanning, M., Lambert-Smith, J., Harbidge, R., Vargas, C., Turnbull, R., Joel Holliday, J., Paleoproterozoic gold deposits of the Loulo district, western Mali: Society of Economic Geologists Special Publication 23, 2020, in press.

Baratoux, L., Metelka, V., Naba, S., Jessell, M. W., Grégoire, M. and Ganne, J., 2011, Juvenile Paleoproterozoic crust evolution during the Eburnean orogeny (~ 2.2–2.0 Ga), western Burkina Faso: *Precambrian Research,* v. 191**,** p. 18-45.

Block, S., Ganne, J., Baratoux, L., Zeh, A., Parra-Avila, L., Jessell, M., Ailleres, L. and Siebenaller, L., 2015, Petrological and geochronological constraints on lower crust exhumation during Paleoproterozoic (Eburnean) orogeny, NW Ghana, West African Craton: *Journal of Metamorphic Geology,* v. 33**,** p. 463-494.

Campbell Mccuaig, T. and Kerrich, R., 1998, P—T—t—deformation—fluid characteristics of lode gold deposits: evidence from alteration systematics. *Ore Geology Reviews,* v. 12**,** p. 381-453.

Craig, H. 1957, Isotopic standards for carbon and oxygen and correction factors for mass-spectrometric analysis of carbon dioxide: *Geochimica et cosmochimica acta,* v. 12**,** p. 133-149.

Da Costa Silva, A. R., Villas, R. N. N., Lafon, J.-M., Craveiro, G. S. and Ferreira, V. P., 2015, Stable isotope systematics and fluid inclusion studies in the Cu–Au Visconde deposit, Carajás Mineral Province, Brazil: implications for fluid source generation: *Mineralium Deposita,* v. 50**,** p. 547-569.

Davis, D., Hirdes, W., Schaltegger, U. and Nunoo, E., 1994, U-Pb age constraints on deposition and provenance of Birimian and gold-bearing Tarkwaian sediments in Ghana, West Africa: *Precambrian Research,* v. 67**,** p. 89-107.

De Kock, G., Armstrong, R., Siegfried, H. and Thomas, E., 2011, Geochronology of the Birim Supergroup of the West African craton in the Wa-Bolé region of west-central Ghana: Implications for the stratigraphic framework: *Journal of African Earth Sciences,* v. 59**,** p. 1-40.

Dia, A., Van Schmus, W. and Kröner, A., 1997, Isotopic constraints on the age and formation of a Palaeoproterozoic volcanic arc complex in the Kedougou Inlier, eastern Senegal, West Africa: *Journal of African Earth Sciences,* v. 24**,** p. 197-213.

Dietrich, D., Mckenzie, J. A. and Song, H., 1983, Origin of calcite in syntectonic veins as determined from carbon-isotope ratios: *Geology,* v. 11**,** p. 547-551.

Eglinger, A., Thébaud, N., Zeh, A., Davis, J., Miller, J., Parra-Avila, L. A., Loucks, R., Mccuaig, C. and Belousova, E., 2017, New insights into the crustal growth of the Paleoproterozoic margin of the Archean Kéména-Man domain, West African craton (Guinea): Implications for gold mineral system: *Precambrian Research,* v. 292**,** p. 258-289.

Eichmann, R. and Schidlowski, M., 1975, Isotopic fractionation between coexisting organic carbon—carbonate pairs in Precambrian sediments: *Geochimica et Cosmochimica Acta,* v. 39**,** p. 585-595.

Elmer, F., White, R. and Powell, R., 2006, Devolatilization of metabasic rocks during greenschist–amphibolite facies metamorphism: *Journal of Metamorphic Geology,* v. 24**,** p. 497-513.
Fontaine, A., Eglinger, A., Ada, K., André-Mayer, A.-S., Reisberg, L., Siebenaller, L., Le Mignot, E., Ganne, J. and Poujol, M., 2017, Geology of the world-class Kiaka polyphase gold deposit, West African Craton, Burkina Faso: *Journal of African Earth Sciences,* v. 126**,** p. 96-122.
Fougerouse, D., Micklethwaite, S., Ulrich, S., Miller, J., Godel, B., Adams, D. T. and Mccuaig, T. C., 2017, Evidence for two stages of mineralization in West Africa's largest gold deposit: Obuasi, Ghana: *Economic Geology,* v. 112**,** p. 3-22.
Fouillac, A., Dommanget, A. and Milési, J., 1993, A carbon, oxygen, hydrogen and sulfur isotopic study of the gold mineralization at Loulo, Mali. *Chemical geology,* v. 106**,** p. 47-62.
Frimmel, H. E. and Hennigh, Q., 2015, First whiffs of atmospheric oxygen triggered onset of crustal gold cycle: *Mineralium Deposita,* v. 50**,** p. 5-23.
Fu, B., Bröcker, M., Ireland, T.R., Holden, P., and Kinsley, L., 2015, Zircon U-Pb, O, and Hf isotopic constraints on Mesozoic magmatism in the Cyclades, Aegean Sea, Greece: Geologische Rundschau, v. 104, p. 75–87.
Gaboury, D., 2013, Does gold in orogenic deposits come from pyrite in deeply buried carbon-rich sediments?: Insight from volatiles in fluid inclusions: *Geology,* v. 41**,** p. 1207-1210.
Ganne, J., De Andrade, V., Weinberg, R. F., Vidal, O., Dubacq, B., Kagambega, N., Naba, S., Baratoux, L., Jessell, M. and Allibon, J., 2011, Modern-Style Plate Subduction Preserved In The Palaeoproterozoic West African Craton: *Nature Geoscience,* v. 5**,** p. 60.
Goldfarb, R. J., André-Mayer, A.-S., Jowitt, S. M. and Mudd, G. M., 2017, West Africa: The world's premier Paleoproterozoic gold province: *Economic Geology,* v. 112**,** p. 123-143.
Goldfarb, R. J. and Groves, D. I., 2015, Orogenic gold: Common or evolving fluid and metal sources through time: *Lithos,* v. 233**,** p. 2-26.
Goldfarb, R. J., Newberry, R. J., Pickthorn, W. J. and Gent, C. A., 1991, Oxygen, hydrogen, and sulfur isotope studies in the Juneau gold belt, southeastern Alaska; constraints on the origin of hydrothermal fluids: *Economic geology,* v. 86**,** p. 66-80.
Golyshev, S.I., Padalko, N.L. and Pechenkin, S.A., 1981, Fractionation of stable oxygen and carbon isotopes in carbonate systems: Geochemistry International v. 18, p. 85-99.
Grenholm, M., Jessell, M. and Thébaud, N., 2019, A geodynamic model for the Paleoproterozoic (ca. 2.27–1.96 Ga) Birimian Orogen of the southern West African Craton–Insights into an evolving accretionary-collisional orogenic system: *Earth-Science Reviews*, v. 192, p. 138-193
Groves, D. I., Goldfarb, R. J., Gebre-Mariam, M., Hagemann, S. and Robert, F., 1998, Orogenic gold deposits: a proposed classification in the context of their crustal distribution and relationship to other gold deposit types: *Ore geology reviews,* v. 13**,** p. 7-27.
Groves, D. I., Santosh, M., Deng, J., Wang, Q., Yang, L. and Zhang, L., 2019, A holistic model for the origin of orogenic gold deposits and its implications for exploration: *Mineralium Deposita***,** pp. 1-18.
Gueye, M., Siegesmund, S., Wemmer, K., Pawlig, S., Drobe, M., Nolte, N. and Layer, P., 2007, New evidences for an early Birimian evolution in the West African Craton: An example from the Kedougou-Kenieba inlier, southeast Senegal: *South African Journal of Geology,* v. 110**,** p. 511-534.
Hein, K. A., 2010, Succession of structural events in the Goren greenstone belt (Burkina Faso): implications for West African tectonics: *Journal of African Earth Sciences,* 56**,** p. 83-94.
Henley, R.W., Norris, R.J., and Paterson, C.J., 1976, Multistage ore genesis in the New Zealand Geosyncline: a history of post-metamorphic lode emplacement: Mineralium Deposita, v. 11, p. 180-196.
Hirdes, W. and Davis, D., 2002, U–Pb geochronology of paleoproterozoic rocks in the southern part of the Kedougou-Kenieba Inlier, Senegal, West Africa: evidence for diachronous accretionary development of the Eburnean province: *Precambrian Research,* v. 118**,** p. 83-99.

Horita, J., 2001. Carbon isotope exchange in the system CO2-CH4 at elevated temperatures: *Geochimica et Cosmochimica Acta,* v. 65**,** p. 1907-1919.

Ickert, R.B., Hiess, J., Williams, I.S., Holden, P., Ireland, T.R., Lanc, P., Schram, N., Foster, J.J. and Clement, S.W., 2008, Determining high precision, in situ, oxygen isotope ratios with a SHRIMP II: Analyses of MPI-DING silicate-glass reference materials and zircon from contrasting granites: Chemical Geology v. 257, p. 114-128.

Jenkin, G. R. T., Linklater, C. and Fallick, A. E., 1991, Modeling of mineral δ18O values in an igneous aureole: Closed-system model predicts apparent open-system δ18O values: *Geology,* v. 19**,** p. 1185-1188.

John, T., Klemd, R., Hirdes, W. and Loh, G., 1999, The metamorphic evolution of the paleoproterozoic (Birimian) volcanic Ashanti belt (Ghana, West Africa): *Precambrian Research,* 98**,** p. 11-30.

Kerrich, R. and Wyman, D., 1990, Geodynamic setting of mesothermal gold deposits: An association with accretionary tectonic regimes: *Geology,* v. 18**,** p. 882-885.

Lambert-Smith, J. S., 2014, The geology, structure and metallogenesis of the world class Loulo-Bambadji Au district in Mali and Senegal, West Africa*:* Unpublished Ph.D. thesis, Kingston upon Thames, UK, Kingston University London, 354 p.

Lambert-Smith, J. S., Lawrence, D. M., Müller, W. and Treloar, P. J., 2016a, Palaeotectonic setting of the south-eastern Kédougou-Kéniéba Inlier, West Africa: New insights from igneous trace element geochemistry and U-Pb zircon ages: *Precambrian Research,* v. 274**,** p. 110-135.

Lambert-Smith, J. S., Lawrence, D. M., Vargas, C. A., Boyce, A. J., Treloar, P. J. and Herbert, S., 2016b, The Gounkoto Au deposit, West Africa: Constraints on ore genesis and volatile sources from petrological, fluid inclusion and stable isotope data: *Ore Geology Reviews,* v. 78**,** p. 606-622.

Lambert-Smith, J. S., Rocholl, A., Treloar, P. J. and Lawrence, D. M., 2016c, Discriminating fluid source regions in orogenic gold deposits using B-isotopes: *Geochimica et Cosmochimica Acta,* v. 194**,** p. 57-76.

Lawrence, D. M., Lambert-Smith, J. S. and Treloar, P. J., 2016, A Review of Gold Mineralization in Mali, In Bouabdellah, M. and Slack, J. F. (eds.) *Mineral Deposits of North Africa.* Springer International Publishing. pp. 327-352.

Lawrence, D. M., Treloar, P. J., Rankin, A. H., Harbidge, P. and Holliday, J., 2013a, The geology and mineralogy of the Loulo mining district, Mali, West Africa: Evidence for two distinct styles of orogenic gold mineralization: *Economic Geology,* v. 108**,** p. 199-227.

Lawrence, D. M., Treloar, P. J., Rankin, A. H., Boyce, A. and Harbidge, P., 2013b, A fluid inclusion and stable isotope study at the Loulo mining district, Mali, West Africa: Implications for multifluid sources in the generation of orogenic gold deposits: *Economic Geology,* v. 108**,** p. 229-257.

Lebrun, E., Thébaud, N., Miller, J., Ulrich, S., Bourget, J. and Terblanche, O., 2016, Geochronology and lithostratigraphy of the Siguiri district: Implications for gold mineralisation in the Siguiri Basin (Guinea, West Africa): *Precambrian Research,* v. 274**,** p. 136-160.

Loh, G., Hirdes, W., Anani, C., Davis, D. W. and Vetter, U. K., 2000, Explanatory Notes for the Geological Map of-Southwest Ghana 1: 100,000-Sekondi (0402A) and Axim (0403B) Sheets.

Mcfarlane, H. B., Ailleres, L., Betts, P., Ganne, J., Baratoux, L., Jessell, M. W., and Block, S., 2019, Episodic collisional orogenesis and lower crust exhumation during the Palaeoproterozoic Eburnean Orogeny: Evidence from the Sefwi Greenstone Belt, West African Craton: *Precambrian Research*, v. 325, p. 88-110.

Mann, J. L., Vocke Jr, R. D. and Kelly, W. R., 2009, Revised δ34S reference values for IAEA sulfur isotope reference materials S-2 and S-3: *Rapid Communications in Mass Spectrometry: An International Journal Devoted to the Rapid Dissemination of Up-to-the-Minute Research in Mass Spectrometry,* v. 23**,** p. 1116-1124.

Markwitz, V., Hein, K. A. A., Jessell, M. W. and Miller, J., 2016, Metallogenic portfolio of the West Africa craton: *Ore Geology Reviews,* v. 78**,** p. 558-563.

Masurel, Q., Thébaud, N., Miller, J. and Ulrich, S., 2017a, The tectono-magmatic framework to gold mineralisation in the Sadiola-Yatela gold camp and implications for the paleotectonic setting of the Kédougou-Kénieba inlier, West Africa: *Precambrian Research,* v. 292**,** p. 35-56.

Masurel, Q., Thébaud, N., Miller, J., Ulrich, S., Hein, K. A., Cameron, G., Béziat, D., Bruguier, O. and Davis, J. A., 2017b, Sadiola Hill: A world-class carbonate-hosted gold deposit in Mali, West Africa: *Economic Geology,* v. 112**,** p. 23-47.

Masurel, Q., Thébaud, N., Miller, J., Ulrich, S., Roberts, M. P. and Béziat, D., 2017c, The Alamoutala Carbonate-Hosted Gold Deposit, Kédougou-Kénieba Inlier, West Africa: *Economic Geology,* v. 112**,** p. 49-72.

Mcfarlane, C. R., Mavrogenes, J., Lentz, D., King, K., Allibone, A. and Holcombe, R., 2011, Geology and intrusion-related affinity of the Morila gold mine, southeast Mali: *Economic Geology,* v. 106**,** p. 727-750.

Mumin, A., Fleet, M. and Longstaffe, F., 1996, Evolution of hydrothermal fluids in the Ashanti gold belt, Ghana; stable isotope geochemistry of carbonates, graphite, and quartz: *Economic Geology,* v. 91**,** p. 135-148.

Norris, R.J. and Henley, R.W., 1976, Dewatering of a metamorphic pile. Geology, v. 4, p. 333-336.

Oberthuer, T., Mumm, A. S., Vetter, U., Simon, K. and Amanor, J. A., 1996, Gold mineralization in the Ashanti Belt of Ghana; genetic constraints of the stable isotope geochemistry: *Economic Geology,* v. 91**,** p. 289-301.

Oberthür, T., Vetter, U., Davis, D. W. and Amanor, J. A., 1998, Age constraints on gold mineralization and Paleoproterozoic crustal evolution in the Ashanti belt of southern Ghana: *Precambrian Research,* v. 89**,** p. 129-143.

Ohmoto, H., 1972, Systematics of sulfur and carbon isotopes in hydrothermal ore deposits: *Economic Geology,* v. 67**,** p. 551-578.

Ohmoto, H. and Rye, R.O., 1979, Isotopes of sulfur and carbon. In: Barnes, H.I. (Editor), Geochemistry of hydrothermal ore deposits. 2nd Edition, John Wiley and Sons, New York, pp. 509-567.

Papineau, D., De Gregorio, B. T., Cody, G. D., Fries, M. D., Mojzsis, S. J., Steele, A., Stroud, R. M. and Fogel, M. L., 2010, Ancient graphite in the Eoarchean quartz–pyroxene rocks from Akilia in southern West Greenland I: Petrographic and spectroscopic characterization: *Geochimica et Cosmochimica Acta,* v. 74**,** p. 5862-5883.

Parra-Avila, L. A., Belousova, E., Fiorentini, M. L., Baratoux, L., Davis, J., Miller, J. and Mccuaig, T. C., 2016, Crustal evolution of the Paleoproterozoic Birimian terranes of the Baoulé-Mossi domain, southern West African Craton: U–Pb and Hf-isotope studies of detrital zircons: *Precambrian Research,* v. 274**,** p. 25-60.

Parra-Avila, L. A., Belousova, E., Fiorentini, M. L., Eglinger, A., Block, S. and Miller, J., 2018, Zircon Hf and O-isotope constraints on the evolution of the Paleoproterozoic Baoulé-Mossi domain of the southern West African Craton: *Precambrian Research,* v. 306**,** p. 174-188.

Parra-Avila, L. A., Bourassa, Y., Miller, J., Perrouty, S., Fiorentini, M. L. and Campbell Mccuaig, T., 2015, Age constraints of the Wassa and Benso mesothermal gold deposits, Ashanti Belt, Ghana, West Africa: *Journal of African Earth Sciences,* v. 112**,** p. 524-535.

Pass, H. E., Cooke, D. R., Davidson, G., Maas, R., Dipple, G., Rees, C., Ferreira, L., Taylor, C. and Deyell, C. L., 2014, Isotope geochemistry of the Northeast zone, Mount Polley alkalic Cu-Au-Ag porphyry deposit, British Columbia: A case for carbonate assimilation: *Economic Geology,* v. 109**,** p. 859-890.

Perrouty, S., Aillères, L., Jessell, M. W., Baratoux, L., Bourassa, Y. and Crawford, B., 2012, Revised Eburnean geodynamic evolution of the gold-rich southern Ashanti Belt, Ghana, with new field and geophysical evidence of pre-Tarkwaian deformations: *Precambrian Research,* v. 204**,** p. 12-39.

Petersson, A., Scherstén, A. and Gerdes, A., 2018, Extensive reworking of Archaean crust within the Birimian terrane in Ghana as revealed by combined zircon U-Pb and Lu-Hf isotopes: *Geoscience Frontiers,* v. 9**,** p. 173-189.

Phillips, G. N. and Powell, R., 1993, Link between gold provinces: *Economic Geology,* v. 88**,** p. 1084-1098.

Phillips, G. N. and Powell, R., 2010, Formation of gold deposits: a metamorphic devolatilization model: *Journal of Metamorphic Geology,* v. 28**,** p. 689-718.

Pitcairn, I. K., Teagle, D. A., Craw, D., Olivo, G. R., Kerrich, R., and Brewer, T. S., 2006, Sources of metals and fluids in orogenic gold deposits: insights from the Otago and Alpine Schists, New Zealand: *Economic Geology*, v. 101, p. 1525-1546.

Pitcairn, I. K., Craw, D., and Teagle, D. A., 2014, The gold conveyor belt: Large-scale gold mobility in an active orogen: *Ore Geology Reviews*, v. 62, p. 129-142.

Riehl, W. and Cabral, A.R., 2018, Meta-evaporite in the Carajás mineral province, northern Brazil: *Mineralium Deposita*, v. 53, p. 895-902.

Robinson, B. W. and Kusakabe, M., 1975, Quantitative preparation of sulfur dioxide, for sulfur-34/sulfur-32 analyses, from sulfides by combustion with cuprous oxide: *Analytical Chemistry,* v. 47**,** p. 1179-1181.

Randgold Resources Ltd., 2017, Annual report. www.randgoldresources.com

Rosenbaum, J. and Sheppard, S. M. F. 1986, An isotopic study of siderites, dolomites and ankerites at high temperatures: *Geochimica et Cosmochimica Acta,* v. 50**,** p. 1147-1150.

Rye, R. O. and Ohmoto, H., 1974, Sulfur and carbon isotopes and ore genesis: a review: *Economic Geology,* v. 69**,** p. 826-842.

Samperton, K. M., Bell, E. A., Barboni, M., Keller, C. B. and Schoene, B., 2017, Zircon age-temperature-compositional spectra in plutonic rocks: *Geology,* v. 45**,** p. 983-986.

Schidlowski, M., Eichmann, R. and Junge, C. E., 1975, Precambrian sedimentary carbonates: carbon and oxygen isotope geochemistry and implications for the terrestrial oxygen budget: *Precambrian Research,* v. 2**,** p. 1-69.

Schwartz, M. and Melcher, F., 2004, The Faleme Iron District, Senegal. *Economic Geology,* v. 99**,** p. 917-939.

Schwinn, G., Wagner, T., Baatartsogt, B. and Markl, G., 2006, Quantification of mixing processes in ore-forming hydrothermal systems by combination of stable isotope and fluid inclusion analyses: *Geochimica et Cosmochimica Acta,* v. 70**,** p. 965-982.

Sharp, Z., 2017, Principles of stable isotope geochemistry (digitalrepository.unm.edu).

Shelton, K. L., 1983, Composition and origin of ore-forming fluids in a carbonate-hosted porphyry copper and skarn deposit; a fluid inclusion and stable isotope study of Mines Gaspe, Quebec: *Economic Geology,* v. 78**,** p. 387-421.

Sheppard, S. M. F., 1986, Chapter 6. Characterization and Isotopic Variations in Natural Waters: *Stable Isotopes in High Temperature Geological Processes.*

Spence-Jones, C. P., Jenkin, G. R. T., Boyce, A. J., Hill, N. J. and Sangster, C. J. S., 2018, Tellurium, magmatic fluids and orogenic gold: An early magmatic fluid pulse at Cononish gold deposit, Scotland: *Ore Geology Reviews,* v. 102**,** p. 894-905.

Strauss, H. and Moore, T., 1992, Abundances and isotopic compositions of carbon and sulfur species in whole rock and kerogen samples: *The Proterozoic biosphere: A multidisciplinary study***,** pp. 709-798.

Taylor, H., 1974, The application of oxygen and hydrogen isotope studies to problems of hydrothermal alteration and ore deposition: *Economic geology,* v. 69**,** p. 843-883.

Taylor, P. N., Moorbath, S., Leube, A. and Hirdes, W., 1992, Early Proterozoic crustal evolution in the Birimian of Ghana: constraints from geochronology and isotope geochemistry: *Precambrian Research,* v. 56**,** p. 97-111.

Thébaud, N., Allibone, A., Masurel, Q., Eglinger, A., Davis, J., André-Mayer, A., Miller, J. And Jessell, M, The Paleoproterozoic (Rhyacian) gold deposits of West Africa: *Society of Economic Geologists Special Publication* 23, 2020, in press.

Tomkins, A. G., 2013, On the source of orogenic gold. *Geology,* v. 41**,** p. 1255-1256.

Trail, D., Bindeman, I. N., Watson, E. B. and Schmitt, A. K., 2009, Experimental calibration of oxygen isotope fractionation between quartz and zircon: *Geochimica et Cosmochimica Acta,* v. 73**,** p. 7110-7126.

Treloar, P., Lawrence, D., Senghor, D., Boyce, A. and Harbidge, P., 2015, The Massawa gold deposit, Eastern Senegal, West Africa: an orogenic gold deposit sourced from magmatically derived fluids? *Geological Society, London, Special Publications,* v. 393**,** p. 135-160.

Tshibubudze, A., Hein, K. A. and Mccuaig, T. C., 2015, The relative and absolute chronology of strato-tectonic events in the Gorom-Gorom granitoid terrane and Oudalan-Gorouol belt, northeast Burkina Faso: *Journal of African Earth Sciences,* v. 112**,** p. 382-418.

Valley, J. W., 1986, Stable isotope geochemistry of metamorphic rocks: *Reviews in Mineralogy and Geochemistry,* v. 16**,** p. 445-489.

Van Hinsberg, V. J., Henry, D. J. and Marschall, H. R., 2011, Tourmaline: an ideal indicator of its host environment: *The Canadian Mineralogist,* v. 49**,** p. 1-16.

Vidal, M., Gumiaux, C., Cagnard, F., Pouclet, A., Ouattara, G. and Pichon, M., 2009, Evolution of a Paleoproterozoic “weak type” orogeny in the West African Craton (Ivory Coast): *Tectonophysics,* v. 477**,** p. 145-159.

White, A., Burgess, R., Charnley, N., Selby, D., Whitehouse, M., Robb, L. and Waters, D., 2014, Constraints on the timing of late-Eburnean metamorphism, gold mineralisation and regional exhumation at Damang mine, Ghana: *Precambrian Research,* v. 243**,** p. 18-38.

Williams, P. J., Barton, M. D., Johnson, D. A., Fontboté, L., De Haller, A., Mark, G., Oliver, N. H. and Marschik, R., 2005, Iron oxide copper-gold deposits: Geology, space-time distribution, and possible modes of origin: *Economic Geology***,** pp. 371-405.

Wyman, D. A., Cassidy, K. F. and Hollings, P., 2016, Orogenic gold and the mineral systems approach: Resolving fact, fiction and fantasy: *Ore Geology Reviews,* v. 78**,** 322-335.

Xavier, R. P., Wiedenbeck, M., Trumbull, R. B., Dreher, A. M., Monteiro, L. V., Rhede, D., De Araújo, C. E. and Torresi, I., 2008, Tourmaline B-isotopes fingerprint marine evaporites as the source of high-salinity ore fluids in iron oxide copper-gold deposits, Carajas Mineral Province (Brazil) : *Geology,* v. 36**,** p. 743-746.

Xue, Y., Campbell, I., Ireland, T. R., Holden, P. and Armstrong, R., 2013, No mass-independent sulfur isotope fractionation in auriferous fluids supports a magmatic origin for Archean gold deposits: *Geology,* v. 41**,** p. 791-794.

Yardley, B. W. and Cleverley, J. S., 2015, The role of metamorphic fluids in the formation of ore deposits: *Geological Society, London, Special Publications,* v. 393**,** p. 117-134.

Zheng, Y.-F., 1993, Calculation of oxygen isotope fractionation in hydroxyl-bearing silicates: *Earth and Planetary Science Letters,* v. 120**,** p. 247-263.

Zheng, Y.-F., 1999, Oxygen isotope fractionation in carbonate and sulfate minerals: *Geochemical Journal,* v. 33**,** p. 109-126.

Table captions

Table 1 – Summary of key characteristics of Au and Fe mineralization in the Loulo District.

Table 2 - Table summarising stable sulfur isotope data from the Loulo Mining District. * - denotes data from Fouillac et al. (1993). † - denotes data from Lawrence et al. (2013b). ‡ - denotes data from Lambert-Smith et al. (2016b).

Table 3 – Table summarising stable carbon and oxygen isotope data from the Loulo Mining District. * - denotes data from Fouillac et al. (1993). † - denotes data from Lawrence et al. (2013b). ‡ - denotes data from Lambert-Smith et al. (2016b).

Table 4 – Chemical and isotopic fluid compositions used for end member components in fluid mixing and fluid-rock reaction models.

Figure captions

Fig. 1. Geological map of the southern West Africa Craton, highlighting the distribution of Au deposits (Modified after Baratoux et al., 2011; Fontaine et al., 2017; Thebaud et al. In Press). Location of major Au deposits are based on those reported in Markwitz et al. (2016), and Goldfarb et al. (2017).

Fig. 2. Geological map of the Loulo Mining District in the south eastern region of the Kédougou-Kéniéba inlier, with studied Au occurrences highlighted. Modified after Lawrence et al. (2013a), and Lambert-Smith et al. (2016c).

Fig. 3. Key alteration and ore mineral textures at Karakaene Ndi. (A) photograph of coarse epidote-albite-calcite vein cross cutting albitized igneous rock with envelopes of dark green actinolite replacement in the wall rock and Fe-rich halos encroaching on the albitized rock. Photomicrographs of (B) albitized wall rock with relict phenocrysts (replaced by albite) (XPL); (C) fine fibrous actinolite replacing wall rock with minor magnetite mineralization (PPL); (D) albitized wall rock overprinted by Fe-rich carbonate and disseminated actinolite with minor pyrite (PPL) and; (E) coarse intergrown epidote and albite in cross cutting vein (XPL). Photographs of ore textures in diamond drill core from Karakaene Ndi showing: (F) massive magnetite replacement with weak disseminated pyrite overprint and; (G) late calcite-pyrite-chlorite vein cross cutting magnetite mineralization.

Fig. 4. Field photographs showing (A) typical marly dolostones country rock with highly deformed calcite veining, argillaceous layers and graphitic material. (B) Ankerite-quartz-pyrite stockwork ore characteristic of the Gara and Gounkoto deposit (highly subordinate in the latter), the P64 satellite, and the Baqata and Kolya exploration targets. (C) Auriferous ankerite-quartz-pyrite veins cross cutting phyllic wall rock alteration at the Yalea deposit. (D) An example of sulfide-bearing carbonate veins with Au concentrations below the detection limit of fire assay in the meter of core sampled. (E) Barren

veining in unaltered and unmineralized Kofi Series metasedimentary country rock. (F) Folded, sulfide-free veining in weakly altered, unmineralized metasedimentary host rock. (G) Sulfide-bearing veins from the Kofi Series with fire assay results below detection limit (<0.01 ppm).

Fig. 5. Histograms showing $\delta^{34}S$ data from pyrite at (A) the Loulo Au deposits (Fouillac et al., 1993, Lawrence et al., 2013b, Lambert-Smith et al., 2016b, Lambert-Smith, 2014b) and diagenetic pyrite from the Kofi series dolostones, (B) the Kabe West, Kolya, Baqata and Bobotie exploration targets, (C) the Karakaene Ndi skarn deposit, with parganetic breakdown between sulfides disseminated in the iron ore and those hosted in cross cutting veins (inset).

Fig. 6. Histograms showing $\delta^{13}C$ data from (A) ankerite and dolomite in auriferous hydrothermal veins, barren hydrothermal veins, and carbonate country rocks from the Loulo-Gounkoto complex, including the Gara, Yalea and Gounkoto mines (data from Fouillac et al., 1993, Lawrence et al., 2013b, Lambert-Smith et al., 2016b); (B) ankerite and dolomite in auriferous and barren hydrothermal veins from the Bambadji exploration targets, Gefa, Boboti, Kabe West, Kolya and Baqata; (C) calcite from late hydrothermal veins at the Karakaene Ndi iron skarn deposit. Fields of typical C-isotope characteristics of Precambrian marine carbonates and organic carbon are indicated (Schidlowski et al., 1975, Eichmann and Schidlowski, 1975). Histograms showing $\delta^{18}O$ data from (D) ankerite and dolomite in auriferous hydrothermal veins, barren hydrothermal veins, and carbonate country rocks from the Loulo-Gounkoto complex; (E) ankerite and dolomite in auriferous and barren hydrothermal veins from the Bambadji exploration targets, Gefa, Boboti, Kabe West, Kolya and Baqata; (F) calcite from late hydrothermal veins at the Karakaene Ndi iron skarn deposit. Number of samples and key is equivalent to (A), (B) and (C).

Fig. 7. $\delta^{18}O$ versus $\delta^{13}C$ plot showing isotopic compositions of ore related carbonate at Au deposits and exploration targets in the Loulo District, in addition to compositional ranges of Kofi Series dolostones and barren carbonate veining. Black curve with open circles represents C-O isotopic compositions expected in carbonates precipitated from a mixture of aqueous-carbonic fluid with a starting composition of $\delta^{18}O$ = 10.2 ‰ and $\delta^{13}C$ = -27 ‰ and a magmatic fluid with a starting composition of $\delta^{18}O$ = 9.4 ‰ and $\delta^{13}C$ = -6 ‰ (red star). Black curve with grey circles represents C-O isotopic values expected in carbonates precipitated from a mixture of the same aqueous-carbonic fluid with a brine of meta-evaporite origin and starting isotopic composition of $\delta^{18}O$ = 16.2 ‰ and $\delta^{13}C$ = -2.6 ‰ (blue star). Red curve represents C-O isotopic fluid values resulting from the magmatic fluid reacting with the Kofi Series dolostones (light grey field; average composition of $\delta^{18}O$ = 21 ‰ and $\delta^{13}C$ = -0.5 ‰). The curve was modelled at 550 °C XCO_2 of 0.11. Blue, violet, and purple curves represent isotopic compositions resulting from reaction between the aqueous-carbonic fluid and the Kofi dolostones at 295, 325, and 400 °C, respectively and at XCO_2 of 0.2. Isotopic compositional ranges for magmatic fluids (red field)

(Ohmoto, 1972) and Precambrian marine carbonates (blue field) (Eichmann and Schidlowski, 1975) are given for reference.

Fig. 8. Cartoon cross section showing (A) Kofi Series metasedimentary rocks, including evaporite bearing dolostone horizons in the west of the Series, these are folded and metamorphosed prior to 2085 Ma, with minor albitisation indicating the presence of early saline brines. (B) Intrusion of the Falémé Batholith from approx. 2085 Ma increases the local geothermal gradient and exsolves magmatic-hydrothermal fluid. This event may both promote devolatilization of the dolostones in the Western Kofi Series and allow water-rock reaction between the magmatic fluids and the evaporite-bearing marly dolostones; this gives rise to a hybridized hypersaline magmatic-evaporitic brine, which circulates through the metasedimentary rocks leading to the development of albitized and tourmalinized rock packages. (C) Between 2085 and 2070 Ma hybrid brines continue to circulate, aqueous-carbonic fluids are introduced along significant structures in the Kofi Series and further magmatism in the Falémé batholith leads to emplacement of small stocks and dikes which extend into the Kofi Series. The aqueous-carbonic fluid unmixes in response to pressure fluctuations, contributing to Au mineralization; at Gara and several other deposits this process is enhanced by partial mixing with hybrid hypersaline brines. Minor amounts of magmatic-hydrothermal fluid derived from dikes cross cutting the Kofi Series may contribute volatiles directly to some of the minor mineralized rock packages in the west of the Loulo Au system. Magnetite skarn deposits simultaneously develop within and adjacent to small dioritic stocks in the Falémé batholith and western Kofi Series.

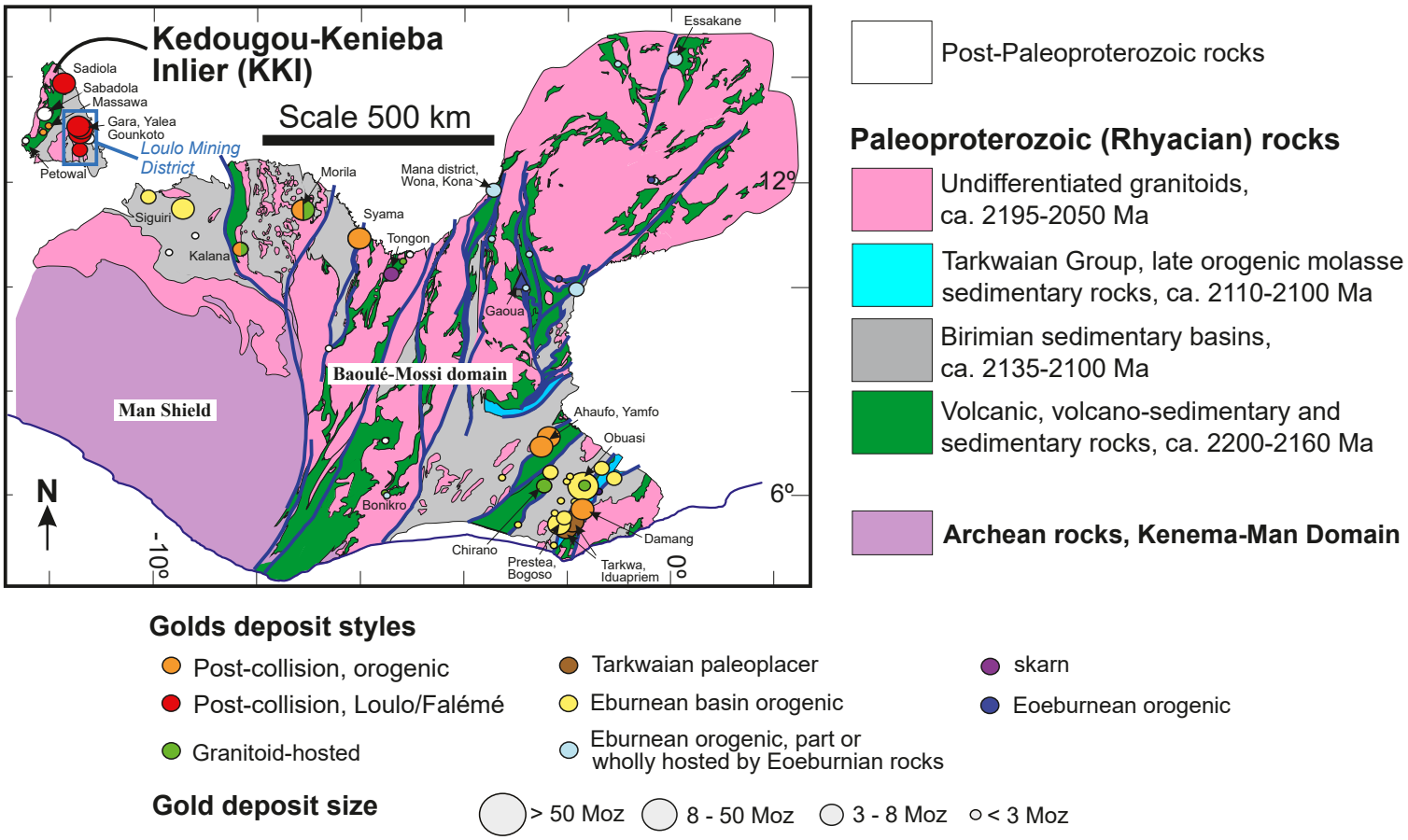
Kedougou-Kenieba Inlier (KKI)
Scale 500 km
Sadiola
Sabadola
Massawa
Gara, Yalea
Gounkoto
Loulo Mining District
Petowal
Essakane
Morila
Mana district, Wona, Kona
Siguiri
Syama
Tongon
Kalana
Gaoua
Baoulé-Mossi domain
Man Shield
Ahaufo, Yamfo
Obuasi
Bonikro
Chirano
Prestea, Bogoso
Tarkwa, Iduapriem
Damang
N
12º
6º
0º
-10º
Post-Paleoproterozoic rocks
Paleoproterozoic (Rhyacian) rocks
Undifferentiated granitoids, ca. 2195-2050 Ma
Tarkwaian Group, late orogenic molasse sedimentary rocks, ca. 2110-2100 Ma
Birimian sedimentary basins, ca. 2135-2100 Ma
Volcanic, volcano-sedimentary and sedimentary rocks, ca. 2200-2160 Ma
Archean rocks, Kenema-Man Domain
Golds deposit styles
Post-collision, orogenic
Post-collision, Loulo/Falémé
Granitoid-hosted
Tarkwaian paleoplacer
Eburnean basin orogenic
Eburnean orogenic, part or wholly hosted by Eoeburnian rocks
skarn
Eoeburnean orogenic
Gold deposit size
> 50 Moz
8 - 50 Moz
3 - 8 Moz
< 3 Moz

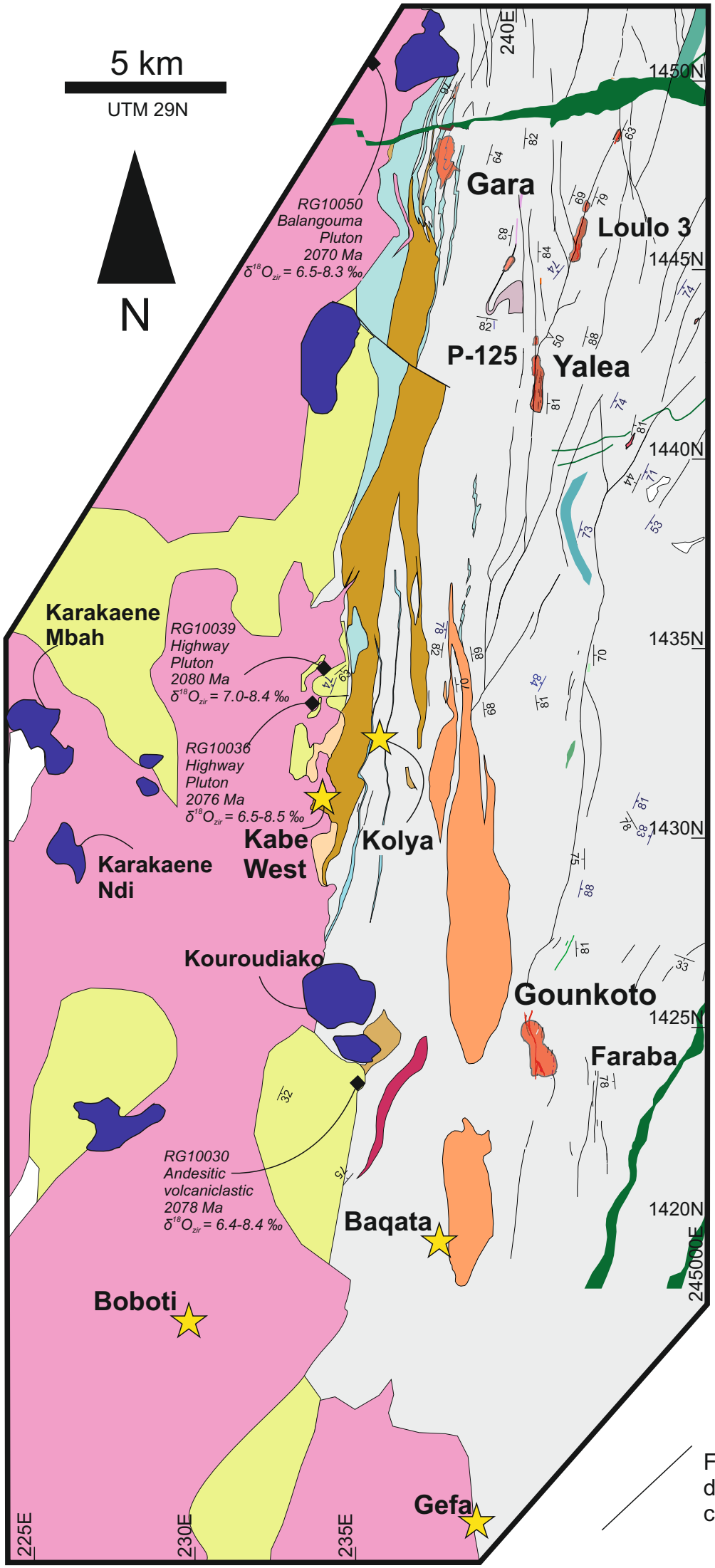

Legend

Post-Birimian lithologies

Dolerite

Altered rocks

Intense albitisation

Strong albitisation (protolith identifiable)

Iron skarn mineralisation

Igneous lithologies

Faleme batholith plutonic rocks

Volcaniclastic and sedimentary rocks

Rhyolitic breccia

Kofi Series

Marly and variably altered marble

Sandstones, siltstones, wackes and argillites with polymict conglomerate

81 Bedding

63 S_{2L} cleavage

◆ *Magmatic and volcanic rock samples with $\delta^{18}O_{zircon}$ data*

★ **Exploration targets**

Au mine

Faults, fractures and shear zones from drilling and outcrop and inferred from chargeability and VTEM data

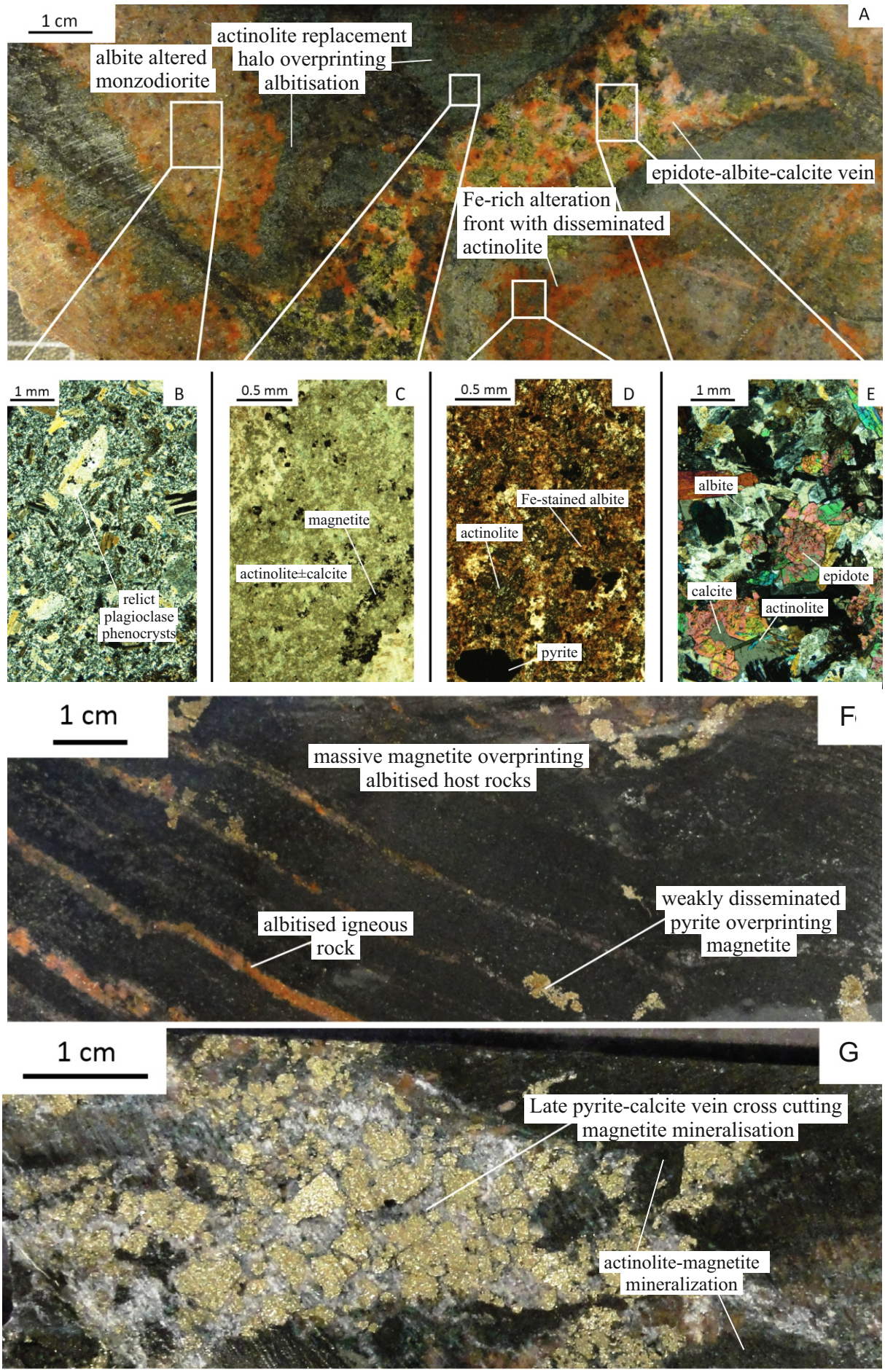
1 cm
A
albite altered monzodiorite
actinolite replacement halo overprinting albitisation
epidote-albite-calcite vein
Fe-rich alteration front with disseminated actinolite
1 mm
B
relict plagioclase phenocrysts
0.5 mm
C
magnetite
actinolite±calcite
0.5 mm
D
Fe-stained albite
actinolite
pyrite
1 mm
E
albite
epidote
calcite
actinolite
1 cm
F
massive magnetite overprinting albitised host rocks
albitised igneous rock
weakly disseminated pyrite overprinting magnetite
1 cm
G
Late pyrite-calcite vein cross cutting magnetite mineralisation
actinolite-magnetite mineralization

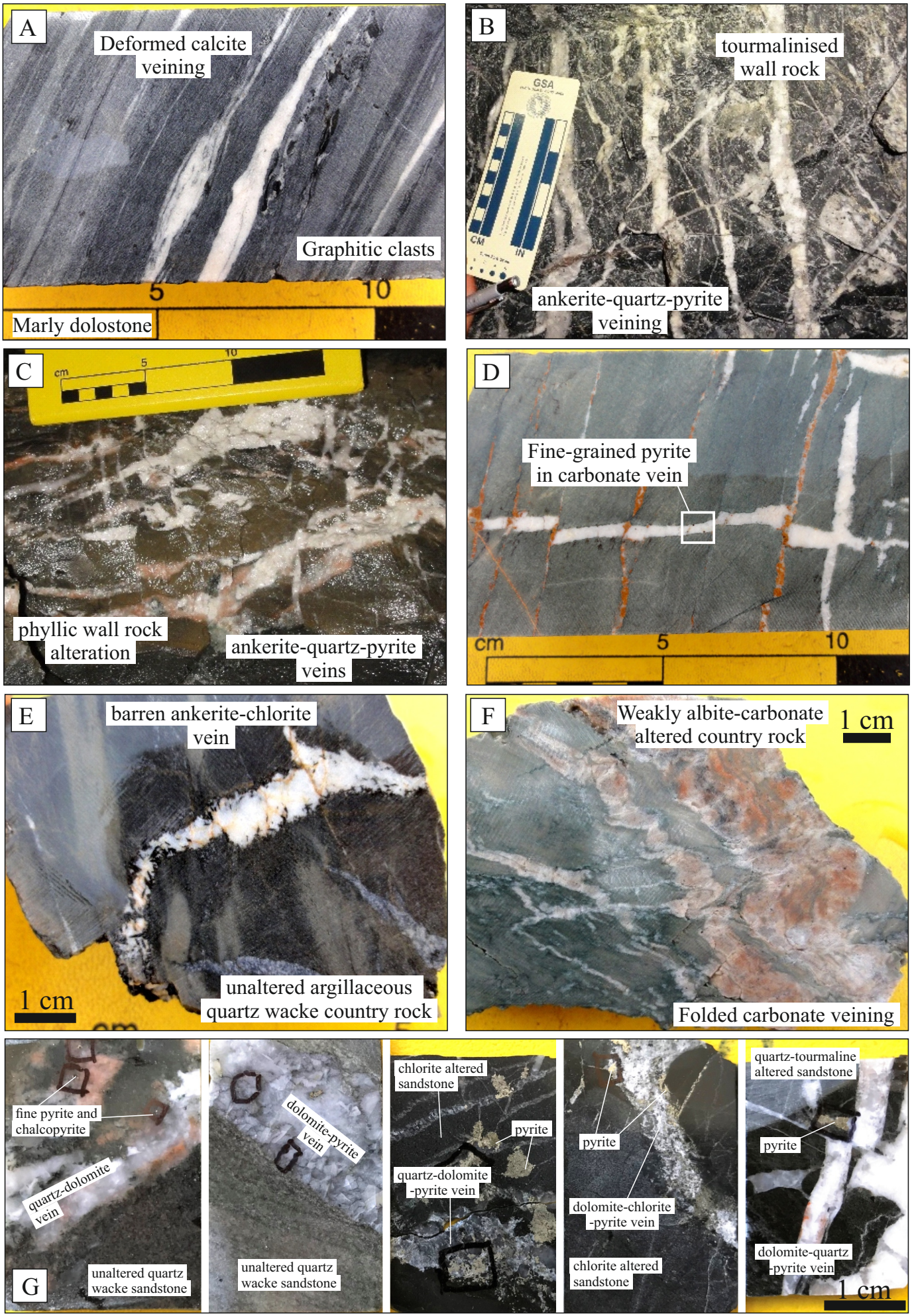
A
Deformed calcite veining
Graphitic clasts
5
10
Marly dolostone
B
tourmalinised wall rock
GSA
CM
IN
ankerite-quartz-pyrite veining
C
cm
5
10
phyllic wall rock alteration
ankerite-quartz-pyrite veins
D
Fine-grained pyrite in carbonate vein
cm
5
10
E
barren ankerite-chlorite vein
1 cm
unaltered argillaceous quartz wacke country rock
F
Weakly albite-carbonate altered country rock
1 cm
Folded carbonate veining
G
fine pyrite and chalcopyrite
quartz-dolomite vein
unaltered quartz wacke sandstone
dolomite-pyrite vein
unaltered quartz wacke sandstone
chlorite altered sandstone
pyrite
quartz-dolomite -pyrite vein
pyrite
dolomite-chlorite -pyrite vein
chlorite altered sandstone
quartz-tourmaline altered sandstone
pyrite
dolomite-quartz -pyrite vein
1 cm

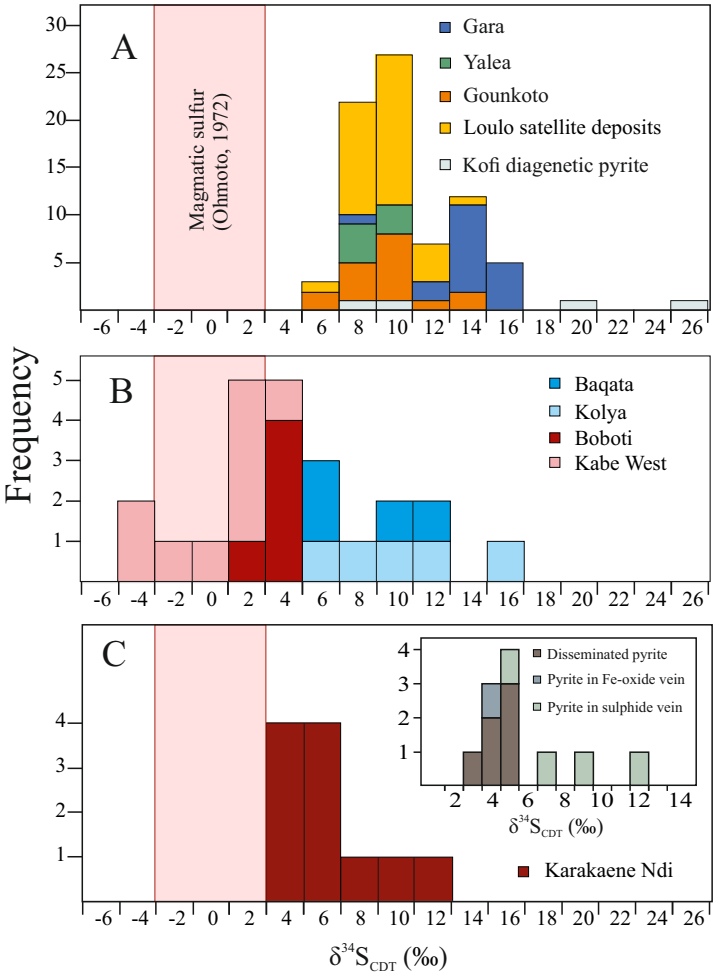
A
Magmatic sulfur
(Ohmoto, 1972)
Gara
Yalea
Gounkoto
Loulo satellite deposits
Kofi diagenetic pyrite
B
Baqata
Kolya
Boboti
Kabe West
C
Disseminated pyrite
Pyrite in Fe-oxide vein
Pyrite in sulphide vein
Karakaene Ndi
Frequency
δ34SCDT (‰)

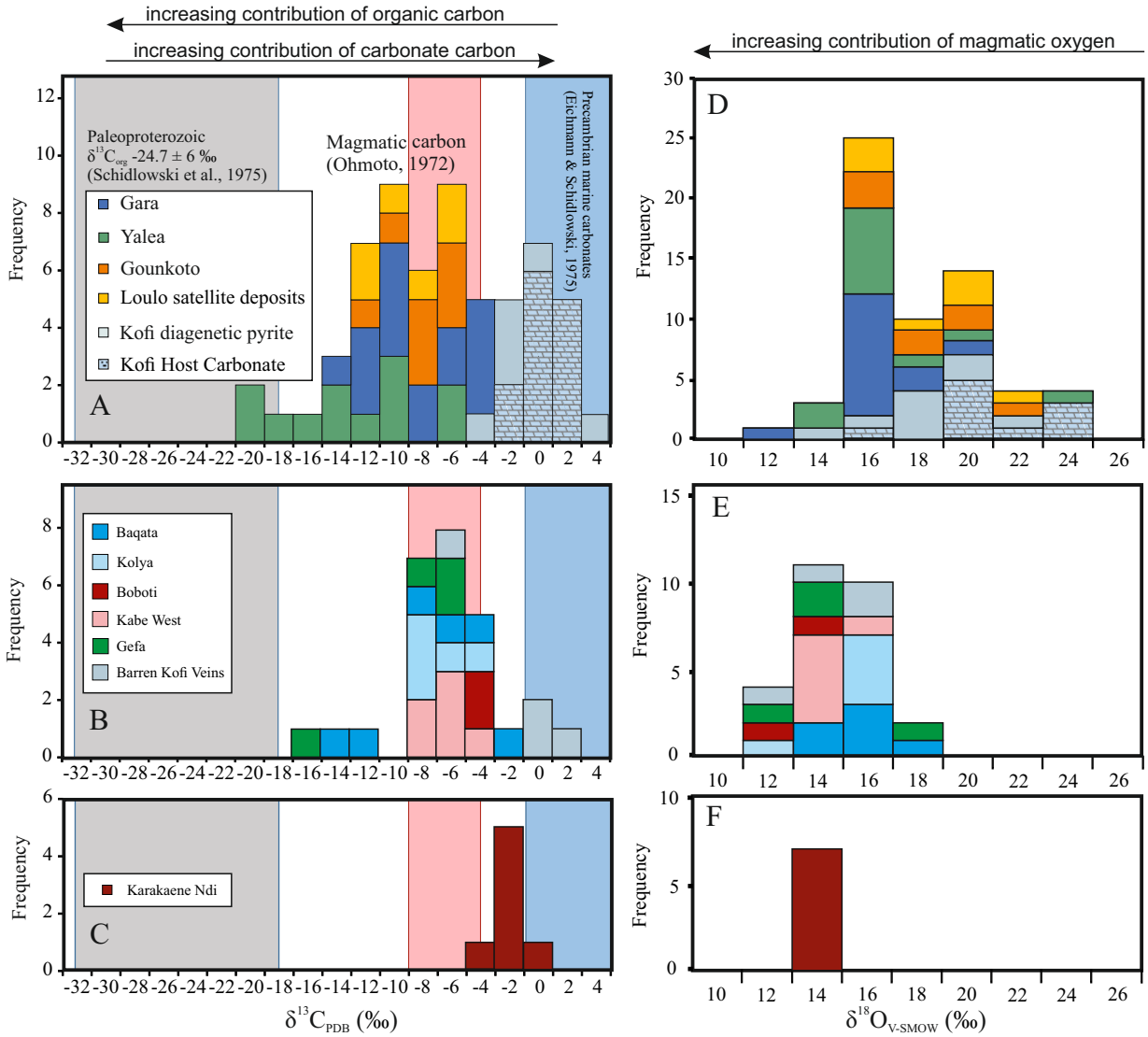
increasing contribution of organic carbon
increasing contribution of carbonate carbon
increasing contribution of magmatic oxygen
Paleoproterozoic
δ13Corg -24.7 ± 6 ‰
(Schidlowski et al., 1975)
Magmatic carbon
(Ohmoto, 1972)
Precambrian marine carbonates
(Eichmann & Schidlowski, 1975)
Gara
Yalea
Gounkoto
Loulo satellite deposits
Kofi diagenetic pyrite
Kofi Host Carbonate
Baqata
Kolya
Boboti
Kabe West
Gefa
Barren Kofi Veins
Karakaene Ndi
A
B
C
D
E
F
Frequency
δ13CPDB (‰)
δ18OV-SMOW (‰)

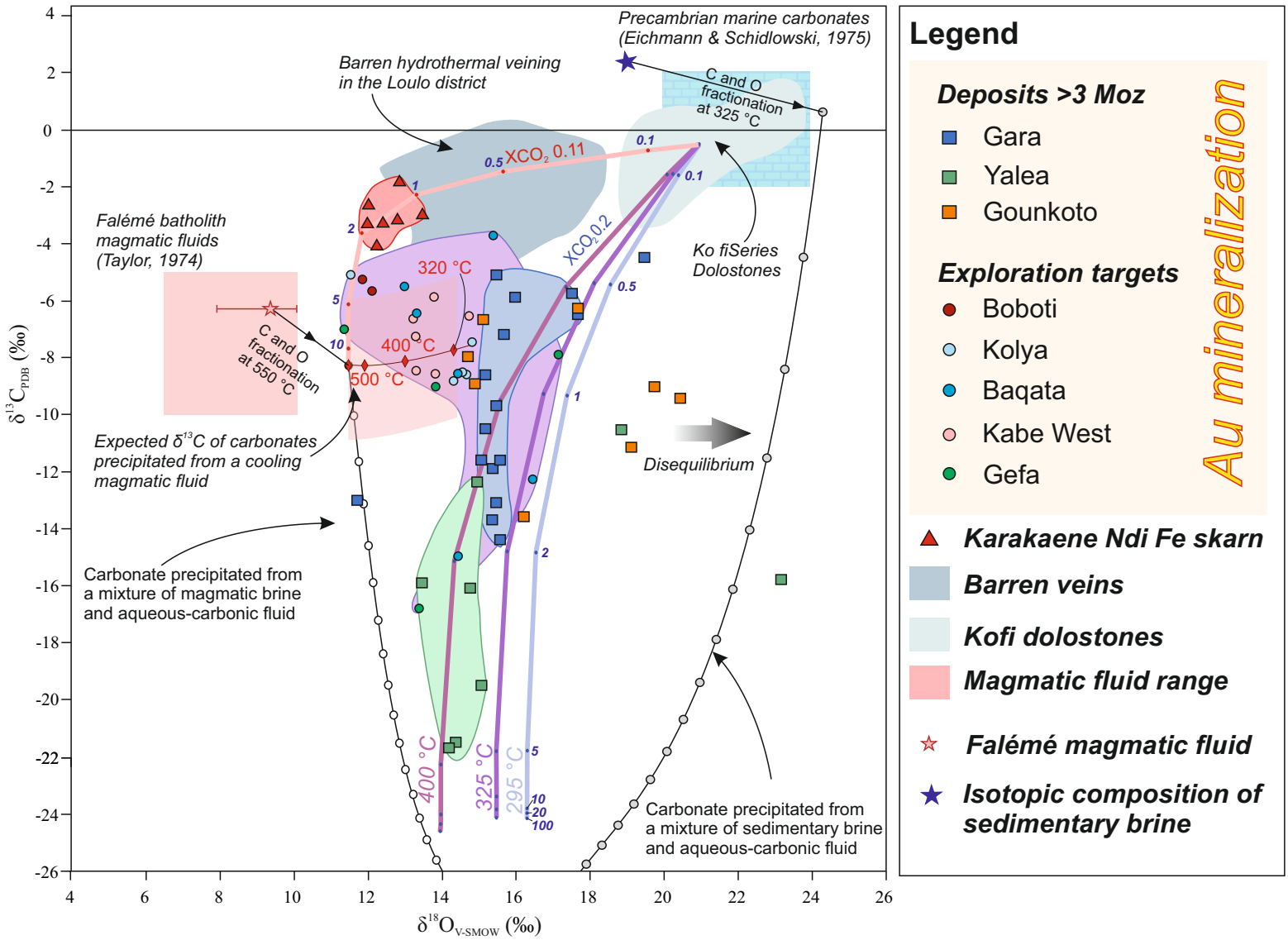
Precambrian marine carbonates
(Eichmann & Schidlowski, 1975)
Barren hydrothermal veining
in the Loulo district
C and O
fractionation
at 325 °C
Falémé batholith
magmatic fluids
(Taylor, 1974)
C and O
fractionation
at 550 °C
Ko fiSeries
Dolostones
Disequilibrium
Expected δ13C of carbonates
precipitated from a cooling
magmatic fluid
Carbonate precipitated from
a mixture of magmatic brine
and aqueous-carbonic fluid
Carbonate precipitated from
a mixture of sedimentary brine
and aqueous-carbonic fluid
XCO2 0.11
XCO2 0.2
320 °C
400 °C
500 °C
400 °C
325 °C
295 °C
δ13CPDB (‰)
δ18OV-SMOW (‰)
Legend
Deposits >3 Moz
Gara
Yalea
Gounkoto
Exploration targets
Boboti
Kolya
Baqata
Kabe West
Gefa
Au mineralization
Karakaene Ndi Fe skarn
Barren veins
Kofi dolostones
Magmatic fluid range
Falémé magmatic fluid
Isotopic composition of
sedimentary brine

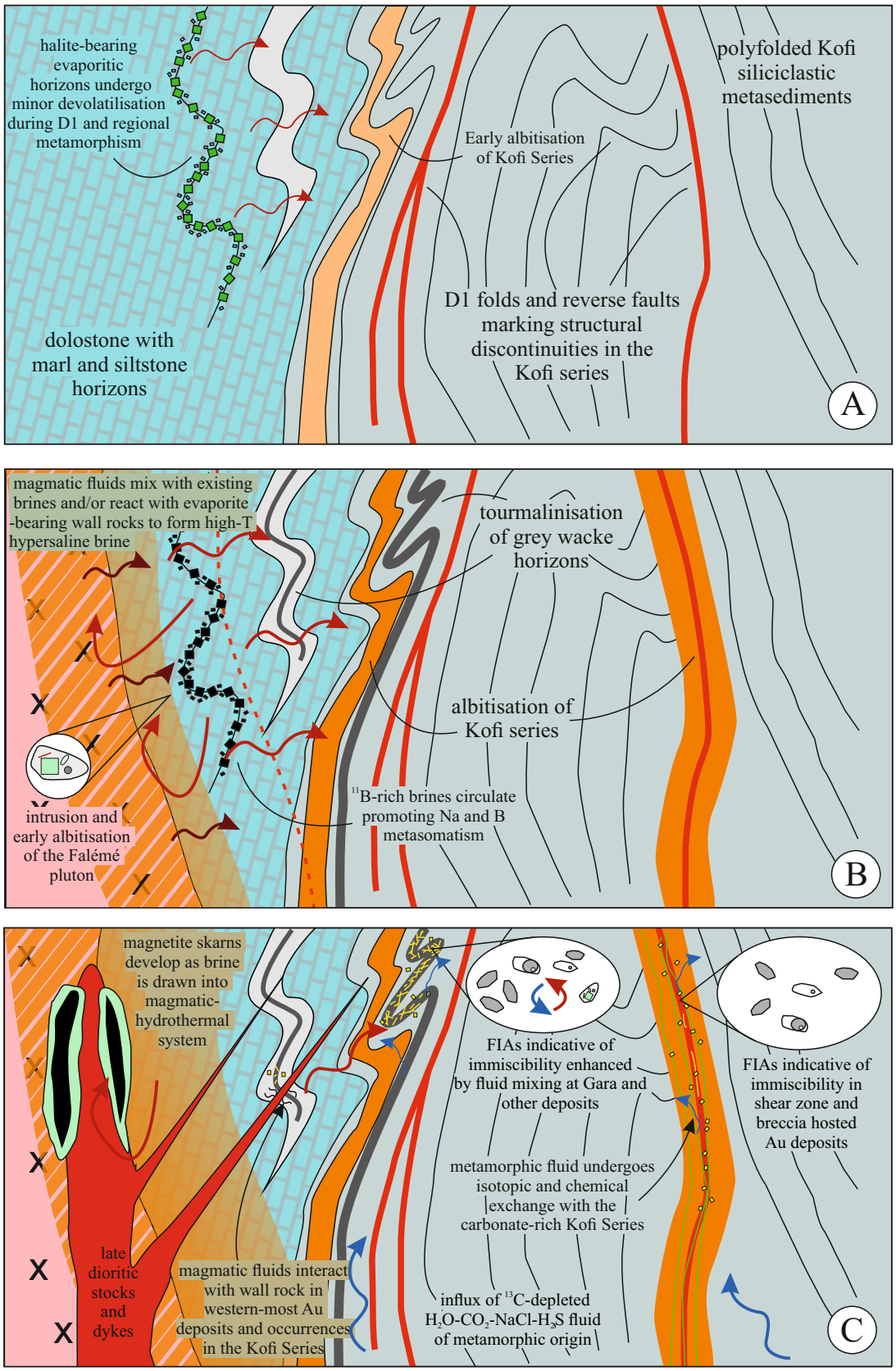
halite-bearing evaporitic horizons undergo minor devolatilisation during D1 and regional metamorphism
dolostone with marl and siltstone horizons
Early albitisation of Kofi Series
D1 folds and reverse faults marking structural discontinuities in the Kofi series
polyfolded Kofi siliciclastic metasediments
A
magmatic fluids mix with existing brines and/or react with evaporite -bearing wall rocks to form high-T hypersaline brine
intrusion and early albitisation of the Falémé pluton
tourmalinisation of grey wacke horizons
albitisation of Kofi series
^{11}B-rich brines circulate promoting Na and B metasomatism
B
magnetite skarns develop as brine is drawn into magmatic-hydrothermal system
late dioritic stocks and dykes
magmatic fluids interact with wall rock in western-most Au deposits and occurrences in the Kofi Series
FIAs indicative of immiscibility enhanced by fluid mixing at Gara and other deposits
metamorphic fluid undergoes isotopic and chemical exchange with the carbonate-rich Kofi Series
influx of ^{13}C-depleted H_2O-CO_2-NaCl-H_2S fluid of metamorphic origin
FIAs indicative of immiscibility in shear zone and breccia hosted Au deposits
C

Ore Body	Key ore textures	Ore mineralogy	Alteration styles	P-T conditions	Constraint	Reference
Gold						
Gara	carbonate-quartz-pyrite vein stockwork	pyrite (± Ni-Co)-monazite-xenotime-scheelite-gold-chalcopyrite-gersdorffite-pentlandite-Ni-pyrrhotite-arsenopyrite-molybdenite	Tourmalinisation and minor albitisation	>340 °C at 1.75 kbar	Fluid inclusions, O-isotope equilibria, arsenpyrite geothermometry	Lawrence et al. (2013a, b)
Yalea	Shear zone hosted sulphide stringers and hydrothermal breccia	arsenian pyite-arsenopyrite-chalcopyrite-gold-pyrrhotite-jamesonite-galena-scheelite-tennantite	Early albitisation and syn-mineralisation chloritisation	320 °C at 1.45 Kbar (5.4 km)	Fluid inclusions, arsenpyrite and chlorite geothermometry, O-isotope equilibria	Lawrence et al. (2013a, b)
Gounkoto	Shear zone hosted sulphide stringers and hydrothermal breccia	pyrite (±As)-arsenopyrite-pyrrhotite-chalcopyrite-magnetite-haematite-gold-monazite-scheelite-gersdorffite-cobaltite-tennantite-altaite-tellurium-callaverite-sylvanite-petzite	Early albitisation and syn-mineralisation chloritisation - minor tourmalinisation	340 °C at 1.4 Kbar (5.2 km)	Fluid inclusions, arsenpyrite and chlorite geothermometry, O-isotope equilibria	Lambert-Smith et al. (2016b)
Faraba	Quartz-dolomite veining, sulfide-chlorite-magnetite veining and disseminated	arsenian pyite - arsenopyrite - magnetite-pyrrhotite - chalcopyrite - gold - tsumoite - altaite - hedleyite - bismuth	Early albitisation and syn-mineralisation chloritisation	-		
Sub-economic gold						
Baqata	carbonate-quartz-pyrite vein stockwork and disseminated	pyrite (± Ni-As) - chalcopyrite-pyrrhotite-monazite-scheelite-xenotime-gold-millerite-polydymite-sternbergite-tellurobismuthite-calaverite-bismuth	Tourmalinisation and albitisation	~315 °C at 1.3 Kbar (4.8 km)	Fluid inclusions, chlorite geothermometry	Lambert-Smith (2014)
Kolya	carbonate-quartz-pyrite vein stockwork	pyrite - chlacopyrite-arsnian pyrite- scheelite-monazite-xenotime-gold-tellurobismuthite-altaite-melonite	Tourmalinisation and minor actinolite replacement	>300 °C	Fluid inclusions (minimum trapping)	Lambert-Smith (2014)
Kabe West	Hydrothermal breccia - carbonate vein stockwork	pyrite (± Ni-Co) - chalcopyrite-monazite-gold-xenotime-altaite-melonite	Albitisation + weak tourmaline	~308 °C	O-isotope equilibria	Lambert-Smith (2014)
Boboti	Hydrothermal veining	pyrite - monazite-gold-haematite-titanite	Weak albitisation	-		
Gefa	carbonate-quartz-pyrite vein stockwork and weakly disseminated	pyrite - chalcopyrite	Tourmalinisation and albitisation	-		
Iron						
Karakaene Ndi	Massive magnetite with late disseminated and vein hosted sulphides	magnetite - haematite - pyrite (N i± As substitution)-apatite-chalcopyrite-monazite-gold-uraninite-bismuth-clausthalite	Early albitisation overpinted by calc-silicate and magnetite replacement	500 °C at 2.5 kbar	Fluid inclusions, O-isotope equilibria	Lambert-Smith (2014)

Deposit / Target	Sample	δ34S(‰ vs. CDT)	Mineral	Notes
Host Rock				
Diagenetic pyrite in dolostone	JLSB09	19.70	Pyrite	
	JLSB07	25.10	Pyrite	
	07YD52	9.00	pyrite	
	07YD89	6.40	pyrite	
Target				
Kolya	JLSB08	9.30	Pyrite	
	JLSB29	14.20	Pyrite	
	JLSB30	7.00	Pyrite	
	JLSB31	4.20	Pyrite	
Boboti	JLSB06	10.20	Pyrite	
	JLSB15	2.60	Pyrite	
	JLSB16	2.20	Pyrite	
	JLSB17	3.90	Pyrite	
	JLSB18	1.70	Pyrite	
	JLSB19	2.10	Pyrite	
Baqata	JLSB12	6.00	Pyrite	
	JLSB25	5.50	Pyrite	
	JLSB27	8.90	Pyrite	
	JLSB26	11.80	Pyrite	
Kabe West	JLSB21	-4.60	Pyrite	
	JLSB23	-3.50	Pyrite	
	KBP01	-4.08	Pyrite	
	KBP02	1.06	Pyrite	
	KBP03	1.36	Pyrite	
	KBP05	-0.65	Pyrite	
	KBP11	1.95	Pyrite	
	KBP12	1.82	Pyrite	
	JLSB22	3.40	Pyrite	
Skarns				
Karakaene Ndi	JLSB01	4.40	Pyrite	Disseminated
	JLSB03	4.20	Pyrite	Disseminated
	JLSB04	3.80	Pyrite	Disseminated
	JLSB05	4.10	Pyrite	Disseminated
	JLSB34 (2)	3.10	Pyrite	Disseminated
	JLSB35	2.80	Pyrite	Disseminated
	JLSB33	4.00	Pyrite	Fe-oxide vein
	JLSB36	7.00	Pyrite	Sulphide vein
	JLSB37	8.07	Pyrite	Sulphide vein
	JLSB38	11.90	Pyrite	Sulphide vein
	JLSB39	4.90	Pyrite	Sulphide vein
Loulo Au deposits				
Faraba	‡FA20	10.60	Pyrite	
	‡FA04	11.40	Pyrite	
	‡FA10	11.90	Pyrite	
	‡FA23	12.60	Pyrite	
	†PT5	15.20	pyrite	
	†PT6	15.50	pyrite	
	†LD13	14.10	pyrite	

	Gara	†LD20	13.60	pyrite
		†LD30	13.80	pyrite
		†LD38	14.50	pyrite
		†LD44	11.70	pyrite
		†LD45	13.30	pyrite
		†LD46	11.50	pyrite
		†LD51	14.30	pyrite
		†LD53	12.50	pyrite
		*C13-100.55	12.10	pyrite
		*C23-26.0	12.90	pyrite
		*C23-198.3b	12.50	pyrite
		*C23-198.55	12.90	pyrite
		*C2-17.75	12.90	pyrite
	Gounkoto	†LD54	7.00	Pyrite
		‡JLS01	8.20	Pyrite
		‡JLS02	7.00	Pyrite
		‡JLS03	8.40	Pyrite
		‡JLS05	9.50	Pyrite
		‡LS06	10.00	Pyrite
		‡JLS10 (2)	7.10	Pyrite
		‡JLS12	12.50	Pyrite
		‡JLS19	7.00	Pyrite
		‡JLS20	9.70	Pyrite
		‡JLS21	12.80	Pyrite
		‡JLS22	5.90	Pyrite
		‡JLS23	8.00	Pyrite
		‡JLS27	9.60	Pyrite
		‡JLS31	10.30	Pyrite
		‡JLS33	9.70	Pyrite
		‡JLS34	6.25	Pyrite
P125	Loulo-3	*C4-18.20	9.20	pyrite
		*C4-21.00	7.80	pyrite
		*C4-16.00	8.90	pyrite
		*C4-18.20	9.20	pyrite
		*C4-21.00	7.80	pyrite
		*C4-16.00	8.90	pyrite
		†PT13	6.70	Pyrite
	P-64	*C3-51.9	8.90	pyrite
		*C1-46.0a	9.20	pyrite
		*C1-46.0b	8.70	pyrite
		*C1-46.0c	8.10	pyrite
		*C12-72.4	6.00	pyrite
		*C2-54.9	6.70	pyrite
		*C1-44.0	6.90	pyrite
		*C1-41.5	7.70	pyrite
		*C1-43.9	7.30	pyrite
		*C3-35.6	7.80	pyrite
		*C14-60.85	6.70	pyrite
		*C12-45.3	8.40	pyrite
		*C14.58.8	8.00	pyrite

	*C4-31.75	9.50	pyrite
	*C4-41.95	10.50	pyrite
	*C4-34.5	8.70	pyrite
	*C10-58.0	8.80	pyrite
	*C4-64.5	8.60	pyrite
	*C4-38.2	9.10	pyrite
	*C13-68.0	9.50	pyrite
	*C6-120.7	9.70	pyrite
	*C14-58.8	7.00	pyrite
	†PT18	7.30	pyrite
	†PT20	8.00	pyrite
	†PT26	8.80	pyrite
Yalea	†07YD60	8.30	pyrite
	†07YD65	7.10	pyrite
	†07YD76	7.70	pyrite
	†YD11	9.20	Pyrite

Deposit/target Name	Sample	δ13CPDB (‰)	δ18OSMOW (‰)	Grade (ppm)	Sample type
Host Rock					
Host Dolostone (Baqata)	JLSB9	-1.44	19.10	<0.01	Host rock
Host Dolostone (Gara)	†G13	1.30	23.20	<0.01	Host rock
	†LD16	-0.40	20.70	<0.01	Host rock
	†LD26	0.10	23.30	<0.01	Host rock
	*C23-26	0.50	22.20	<0.01	Host rock
Host Dolostone (Gounkoto)	‡JLS11	-0.25	19.75	<0.01	Host rock
	‡JLS32	-3.13	19.26	<0.01	Host rock
Host Dolostone (Kolya)	JLSB7	1.11	15.07	<0.01	Host rock
Host Dolostone (Yalea)	†07YD52	-2.90	20.00	<0.01	Host rock
	†07YD53	0.40	19.90	<0.01	Host rock
Barren veins					
Baqata	JLSB10	-1.74	15.31	<0.01	Vein
Gara	†G39	-0.20	17.40	<0.01	Vein
	†G40	-1.70	21.10	<0.01	Vein
	*C13-114.7	-2.00	15.10	<0.01	Vein
	*C23-84	3.80	16.90	<0.01	Vein
Gounkoto	‡JLS18	-2.35	18.23	<0.01	Vein
	‡JLS29	-0.49	18.18	<0.01	Vein
Kolya	JLSB24	0.22	15.21	<0.01	Vein
Yalea	†07YD90	-1.70	16.40	<0.01	Vein
Loulo Au deposits					
Gara	†PT5	-10.50	15.20	3.36	Vein
Gara	†PT9	-11.90	15.40	86.40	Vein
Gara	†LD13	-13.70	15.40	31.40	Vein
Gara	†LD20	-11.60	15.60	90.30	Vein
Gara	†LD31	-13.10	15.50	6.20	Vein
Gara	†LD32	-9.70	15.50	27.80	Vein
Gara	†LD44	-14.40	15.60	8.20	Vein
Gara	†LD45	-11.60	15.10	4.65	Vein
Gara	†LD46	-8.60	15.20	26.80	Vein
Gara	*C13-100.55	-5.90	16.00	-	Vein
Gara	*C23-198.3a	-6.50	17.70	-	Vein
Gara	*C23-198.3b	-4.50	19.50	-	Vein
Gara	*C14-112.5	-5.10	15.50	-	Vein
Gara	*C6-41	-7.20	15.70	-	Vein
Gounkoto	‡JLS06	-11.15	19.15	35.10	Vein
Gounkoto	‡JLS12	-13.60	16.25	7.80	Vein
Gounkoto	‡JLS25	-6.30	17.71	-	Vein
Gounkoto	‡JLS26	-9.44	20.47	-	Vein
Gounkoto	‡JLS28	-6.68	15.16	<0.01	Vein
Gounkoto	‡JLS33	-8.93	14.92	2.90	Vein
Gounkoto	‡JLS34	-9.03	19.77	0.26	Vein
Gounkoto	‡JLS35	-7.99	14.73	0.04	Vein
Yalea Main	†07YD69	-15.80	23.20	15.98	Vein
Yalea Main	†08YD10	-19.50	15.10	-	Vein
Yalea Main	†07YD71	-21.50	14.40	9.43	Wall rock alteration
Yalea Main	†07YD76	-21.70	14.20	5.51	Wall rock alteration
Yalea Main	†08YD24	-15.90	13.50	5.51	Wall rock alteration
Yalea Main	†08YD33	-16.10	14.80	7.80	Wall rock alteration
Faraba	FA20	-6.63	15.42	4.57	Vein
Faraba	FA6	-13.20	20.50	0.34	Vein
Faraba	FA7	-12.20	18.20	0.45	Vein
Faraba	FA12	-10.90	18.50	4.98	Vein

P-64	*C2-52	-7.00	16.90	-	Vein
P-64	*C4-75.5	-8.50	19.10	-	Vein
Target					
Baqata	JLSB11	-3.74	15.42	<0.01	Vein
Baqata	JLSB26	-14.97	14.47	0.13	Vein
Baqata	JLSB28	-8.58	14.46	<0.01	Vein
Baqata	JLSBP10	-6.46	13.35	<0.01	Vein
Baqata	JLSBP12	-5.53	13.03	<0.01	Vein
Baqata	JLSBP17	-12.28	16.48	<0.01	Vein
Boboti	JLSB17	-5.27	11.88	0.04	Vein
Boboti	JLSB18	-5.68	12.15	<0.01	Vein
Gefa	JLSBP44	-16.80	13.41	0.01	Vein
Gefa	JLSBP46	-7.92	17.18	0.01	Vein
Gefa	JLSBP51	-7.02	11.39	0.01	Vein
Gefa	JLSBP55	-9.03	13.86	0.01	Vein
Kabe West	JLSB21	-7.27	13.32	11.53	Vein
Kabe West	JLSB22	-8.47	13.34	0.56	Vein
Kabe West	KBP01	-6.55	14.77	11.33	Vein
Kabe West	KBP03	-5.88	13.82	2.05	Vein
Kabe West	KBP06	-8.58	13.85	0.20	Vein
Kabe West	KBP12	-6.66	13.25	0.01	Vein
Kolya	JLSB29	-7.47	14.85	0.39	Vein
Kolya	JLSB30	-8.84	14.35	0.16	Vein
Kolya	JLSB31	-8.52	14.58	0.08	Vein
Kolya	JLSB32	-8.60	14.69	0.60	Vein

	wt. % NaCl equiv.	X_{H2O}	X_{NaCl}	X_{CO2}	m_{H2O}	m_{NaCl}	m_{CO2}	$\delta^{13}C_i$ (‰)	$\delta^{18}O_i$ (‰)
Kofi Series evaporite brine	41.70	0.70	0.25	0.05	38.86	4.28	1.14	1.80	17.25
Metamorphic fluid	6.10	0.78	0.02	0.20	43.19	0.38	4.54	-27.00	10.20
Magmatic Fluid	3.30	0.82	0.02	0.16	45.67	0.30	3.64	-6.00	9.40

3.5E+08